PERGAMON

International Journal of Multiphase Flow 25 (1999) 257–305

International Journal of Multiphase Flow

A polydisperse model for bubbly two-phase flow around a surface ship

P.M. Carrica *, D. Drew, F. Bonetto, R.T. Lahey Jr

Center for Multiphase Research, Rensselaer Polytechnic Institute, Troy, NY 12180-3590, U.S.A.

Received 29 October 1996; received in revised form 15 July 1998

Abstract

A three dimensional polydisperse model for bubbly two-phase flow around a surface ship is presented. The Boltzmann equation for the bubble mass probability density function is evaluated using a multigroup approach with groups of constant bubble mass. The intergroup transfer mechanisms are bubble breakup, coalescence and the dissolution of air into the ocean, and their effects on the two-phase flow field are analyzed. A three dimensional two-fluid model is used for each bubble mass group to calculate the group's average gas velocity, resulting in four scalar equations per group. The air entrainment process is modeled using simulated breaking bow waves and the steady-state evolution of the gas bubbles for zero Froude number is obtained. It was found that intergroup transfer is very important in these flows. Some of the research areas that need further improvement for the numerical prediction of polydisperse two-phase flow around a ship have been identified and are discussed.

Keywords: 3-D two-phase flow; Bubble distribution; Coalescence; Breakup; Dissolution; Ship hydrodynamics

1. Introduction

The bubbly two-phase flow around a surface ship has attracted increasing attention since World War II. On one hand, the presence of bubbles can modify important design parameters such as ship drag, the wave fields and propeller efficiency. On the other hand, the bubbly wake and the signature generated by the ship strongly depend on the two-phase flow in the region close to the ship's hull. The presence of bubbles in the far-field wake can be determined by measuring acoustic attenuation in the water, and the acoustic response will depend on the

* Corresponding author. Current address: Centro Atómico Bariloche and Instituto Balseiro, 8400, Bariloche, Argentina.

0301-9322/99/$ - see front matter
PII: S0301-9322(98)00047-0

bubble size distribution and the population of bubbles present in the wake. Additionally, the bubbly wake shows at the surface of the sea a characteristic signature of 'white water'. Both the bubbly wake and the white water can be used to detect and identify surface ships from underwater and satellites, respectively.

Bubbles will be present around a ship due to the air entrained in the liquid by the effect of the ship's movement and because of the air already present in the ocean due to wind-induced breaking and spilling waves. Breaking bow and stern waves, spilling waves, boundary layer air entrainment and propeller cavitation and/or ventilation are some of the ship-induced air bubble production mechanisms. There is a fair amount of uncertainty in these air entrainment mechanisms (Melville, 1996). One purpose of this paper is to present a three dimensional model for the transport of bubbles so that sensitivity of the flow to bubble sources can be assessed.

The problem of monodisperse bubbly flow around a ship with background ocean air under non-zero Froude number conditions was studied by Carrica et al. (1997), and the effect of the bubble size in a monodisperse population was presented by Paterson et al. (1996), for the case of simulated breaking waves. In both cases the studies were performed using the geometry of a typical naval combatant, U.S. Navy frigate FF-1052, shown in Fig. 1. This ship offers a complex geometry with a bulbous bow and transom stern, and it has been extensively studied numerically for single-phase flows with and without a propeller (Paterson et al., 1996; Stern et al., 1996), and with zero and non-zero Froude number boundary conditions at the free-surface. Some experimental data also exists for the case of single-phase flow, for a scale-model FF-1052 (see for instance Rattcliffe and Lindenmuth, 1990 or Day and Hurwitz, 1980). As pointed out by Carrica et al. (1997) no experimental published data are available for the case of two-phase flow around a ship. Some studies of the acoustic response in the far wake have been

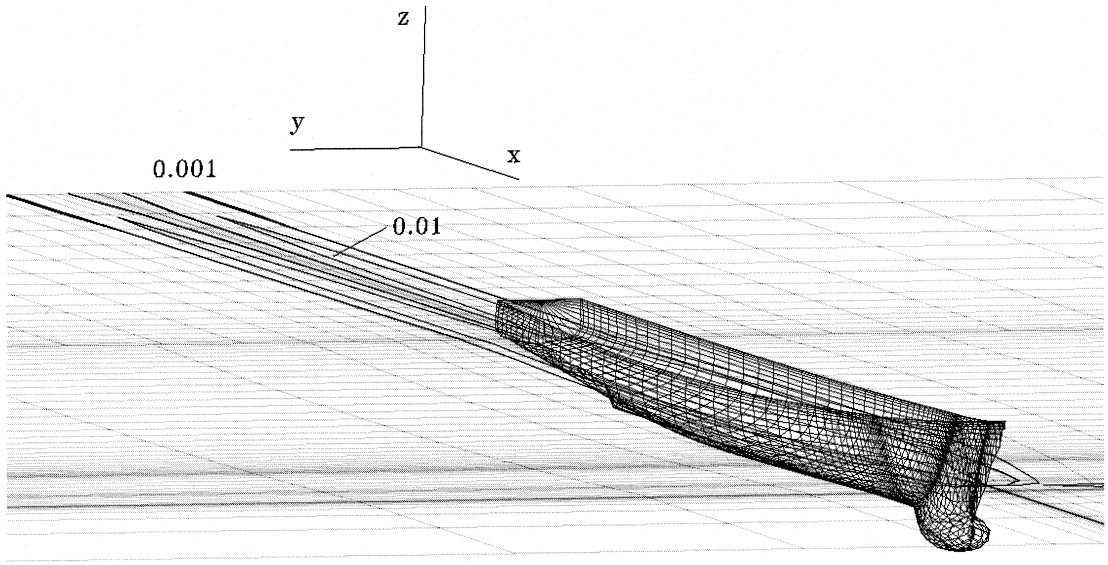

Fig. 1. U.S. Navy FF-1052 and free surface. The contour lines represent constant gas volume fraction.

performed, several ship lengths behind the stern (Hyman, 1994), but little can be inferred about the two-phase flow around the ship from these experiments. This lack of experimental results is not surprising, considering that model-scale ships do not entrain bubbles and data acquisition at full-scale is very complex and expensive. As a part of a program on bubbly wakes, the Navy is expected to perform, in the future, carefully designed experiments with two-phase flow in model-scale ships.

One of the main conclusions of the previous works is that it is necessary to develop the ability to calculate polydisperse bubble populations to properly predict the two-phase flow around a ship, because small and large bubbles behave completely different. The reason for this can be inferred from the two-fluid model equations that govern the motion of the bubbles. The three-dimensional two-fluid model consists of equations for the conservation of mass and momentum for the continuous (liquid) and dispersed (bubbles) phases. Among the terms included in the dispersed phase momentum equations are the virtual mass, drag, pressure, lift and buoyancy forces. Since many of these terms depend on the bubble volume and shape, one of the problems in bubbly flows is the determination of the bubble size at each position in the flow. Moreover, the bubble size distribution can be so broad that the behavior of large and small bubbles is completely different, as occurs in many buoyancy driven flows. It has been shown in the work by Paterson et al. (1996) that in the case of the flow around the ship, big bubbles tend to accumulate below the hull because they rise faster than small ones. Attempts to account for the bubble size distribution in bubbly flows have been made in the past (Guido Lavalle et al., 1994; Sanz et al., 1995). In this paper a more general approach was developed focusing on the bubbly flow around a surface ship.

The calculation of a three dimensional polydisperse flow is a formidable task that was considered impossible with the computational resources available only a few years ago. Even though the computers have improved considerably, the physical modeling has not followed and more work is necessary on some very complex areas such as bubble breakup and coalescence in presence of surfactants, as in the case of salt water.

In this paper we present a three dimensional polydisperse two-fluid model suitable for the prediction of two-phase bubbly flow around a surface ship. The model was solved using a multigroup approach for the case of simulated breaking waves in a U.S. Navy FF-1052 under zero Froude number conditions (flat surface). The model accounts for intergroup transfer through bubble coalescence, dissolution and breakup. The weaknesses of the model are noted through the identification of the most crucial points needing further research to reliably predict two-phase flow around a surface ship.

2. Mathematical modelling

2.1. The distribution function and the bubble transport equation

The statistical description of two-phase flows is developed based on the Boltzmann theory of disperse gases. The fundamental variable is the bubble distribution function $f(\boldsymbol{\phi}, \mathbf{r}, t)$, defined so that the number of bubbles with internal variables in the range $\boldsymbol{\phi}, \boldsymbol{\phi} + \mathrm{d}\boldsymbol{\phi}$), located in a volume $\mathrm{d}\mathbf{r}$ around a spatial location $\mathbf{r}$ at time t is $f(\boldsymbol{\phi}, \mathbf{r}, t)\,\mathrm{d}\mathbf{r}\,\mathrm{d}\boldsymbol{\phi}$. The internal variables are

those relevant for a particular problem, and in general flows with deformed bubbles, the bubble volume, surface area, mean perimeter and velocity must be specified (Sanz et al., 1995). For instance, if some interfacial phenomenon is taking place, such as evaporation or condensation, the interfacial area and the velocity are important. Nevertheless, in many bubbly flows the relationship between bubble volume and the other internal variables are known, or the dependence is single-valued. For instance, we will assume that all the bubbles of volume v have exactly the same area s, the same velocity $\mathbf{u}_g$ and the same mean perimeter, $\bar{P}$. This approximation is particularly reasonable when the bubbles are small and close to spherical. In this case (spherical bubbles) the relationships between the bubble volume and the other internal variables are:

$$\begin{aligned} s &= (36\pi)^{1/3} v^{2/3}, \\ \bar{P} &= (6\pi^2 v)^{1/3}, \\ \mathbf{u}_g &= \mathbf{u}_g(v). \end{aligned} \tag{1}$$

For the sake of simplicity, all the derivations will be made assuming that all the relevant internal variables can be calculated in some way from the bubble mass, so the bubble distribution function is described by the bubble mass, position and time. Under these conditions, we characterize the gas/liquid flow field by a distribution function $f(m, \mathbf{r}, t)$ such that $f(m, \mathbf{r}, t)\, \mathrm{d}m\, \mathrm{d}\mathbf{r}$ is the number of bubbles with mass between m and $m + \mathrm{d}m$, at time t and within $\mathrm{d}\mathbf{r}$ of vector position $\mathbf{r}$. A similar approach, but using the particle volume as internal variable, is frequently used in the theory of aerosols in which the gas is the continuous phase (Williams and Loyalka, 1991), and in chemical engineering to model population distributions (Coulaloglou and Tavlarides, 1976; Ramkrishna, 1985) and was applied to incompressible bubbly two-phase flows by Guido Lavalle et al. (1994) and Sanz et al. (1995). Notice that both formulations are completely equivalent in the case of incompressible gases. In the case of flows where compressibility effects in the gas are important (as is the case of the flow around a ship) the use of the mass as an internal variable is advantageous because it is conserved under pressure changes. By taking the mass moments of the distribution function we obtain the following important two-phase flow parameters:

bubble number density

$$N(\mathbf{r}, t) = \int_0^\infty f(m, \mathbf{r}, t)\, \mathrm{d}m; \tag{2}$$

interfacial area density

$$A_i'''(\mathbf{r}, t) = \int_0^\infty A(m, \mathbf{r}) f(m, \mathbf{r}, t)\, \mathrm{d}m \tag{3}$$

where $A(m, \mathbf{r})$ is the interfacial area of a bubble having mass m at the location $\mathbf{r}$;

bubble mass density

$$\varepsilon_m(\mathbf{r}, t) = \int_0^\infty m f(m, \mathbf{r}, t)\, \mathrm{d}m. \tag{4}$$

The gas volume fraction, or void fraction, is related to the mass density by:

$$\varepsilon(\mathbf{r}, t) = \frac{\varepsilon_m(\mathbf{r}, t)}{\rho_g(\mathbf{r}, t)} \tag{5}$$

where $\rho_g(\mathbf{r}, t)$ is the local gas density which includes the effects of the local pressure. The effect of the surface tension has been neglected for the calculation of the void fraction, due to the small contribution of the small bubbles to the total void fraction. However, surface tension is accounted for in the calculation of the dissolution of bubbles.

In general, the evaluation of the distribution function is described by a partial differential equation, with its boundary and initial conditions and with appropriate laws accounting for the interaction between the bubbles with the surrounding liquid and with each other. Assuming that the bubble velocity for a given size is known,

$$\mathbf{u} = \mathbf{u}(m, \mathbf{r}, t); \tag{6}$$

we can write the conservation equation, i.e. the Boltzmann transport equation for the bubble size distribution function (Guido Lavalle et al., 1994):

$$\frac{\partial f(m, \mathbf{r}, t)}{\partial t} + \frac{\partial}{\partial x_j}[u_j(m, \mathbf{r}, t) f(m, \mathbf{r}, t)] + \frac{\partial}{\partial m}\left[\frac{\mathrm{d}m}{\mathrm{d}t} f(m, \mathbf{r}, t)\right] = \beta(m, \mathbf{r}, t) + \chi(m, \mathbf{r}, t) + S(m, \mathbf{r}, t) \tag{7}$$

where β is the net source due to bubble breakup, χ is the net bubble source due to coalescence and S is a bubble production term. The third term on the left-hand side is related to the mass change of the bubbles that is caused by condensation, evaporation or dissolution. This last term is quite important in our case.

If we consider only binary interactions (i.e. a broken bubble splits into two smaller ones and two bubbles can coalesce to form a bigger one), the bubble breakup term can be written as:

$$\beta(m, \mathbf{r}, t) = \int_m^\infty b(m, m'' \mid m') f(m', \mathbf{r}, t)\, \mathrm{d}m' - \int_0^m b(m', m'' \mid m) f(m, \mathbf{r}, t)\, \mathrm{d}m' \tag{8}$$

where $b(m, m''|\mathrm{m}')$ is the breakup kernel and represents the probability per unit time and mass that a bubble of mass m' splits creating a bubble of mass m'' and a bubble of mass m. This probability is dependent on position through turbulence, shear stress, etc. (Clift et al., 1978).

As no mass is lost or gained in the breakup or coalescence processes, we can use mass conservation to rewrite the bubble breakup term as:

$$\beta(m, \mathbf{r}, t) = \int_m^\infty b(m, m' - m \mid m', \mathbf{r}, t) f(m', \mathbf{r}, t)\, \mathrm{d}m' - \int_0^m b(m', m - m' \mid m, \mathbf{r}, t) f(m, \mathbf{r}, t)\, \mathrm{d}m'. \tag{9}$$

Using similar assumptions as in the breakup term, the coalescence term can be written as:

$$\chi(m,\mathbf{r},t)=\frac{1}{2}\int_0^m \zeta(m-m',m')T(m-m',m',\mathbf{r},t)\,\mathrm{d}m' - \int_0^\infty \zeta(m',m)T(m,m',\mathbf{r},t)\,\mathrm{d}m' \tag{10}$$

where the kernel $T(m-m',\ m',\ \mathbf{r},\ t)$ gives the collision probability per unit time between bubbles of mass m' and m and $\zeta(m,\ m')$ is the probability of coalescence if a collision occurs.

2.2. Bubble collision and coalescence

The coalescence of bubbles occurs after sufficient draining of the liquid film that is formed between two or more bubbles which are in contact. Therefore, two conditions must be met in order to have coalescence between two (or more) bubbles: the bubbles must be in contact (i.e. must collide), and they must remain in contact long enough to allow the liquid film to drain out (Marrucci, 1969). If a collision occurs, coalescence may not happen, however momentum transfer between the colliding bubbles occurs. This phenomenon can be important in regions where the gas volume fraction is high and the presence of surfactants can inhibit coalescence, as in the case of oceanic waters. Since the gas density is much smaller than the liquid density, in this work we will not consider momentum transfer due to collisions between particles that do not coalesce. Additionally, only binary collision events will be considered.

The collision probability is caused by a relative velocity between the bubbles. This relative velocity can be caused by any process that causes differences in the average velocities of the bubbles, such as gravitational and transport forces and velocity gradients, or by processes that cause turbulent or chaotic motions.

Using a geometric analysis, Sanz (1993) found that the collision probability due to the average difference in velocity between the bubbles for a dense (i.e. high void fraction) bubbly flow can be approximated as:

$$T_{\mathrm{U_r}}(m,m')\,\mathrm{d}m\,\mathrm{d}m' = \varepsilon_\mathrm{c}\frac{\pi u_\mathrm{r}(m,m')[R_\mathrm{b}(m)+R_\mathrm{b}(m')]^2}{(\varepsilon_\mathrm{c}-\varepsilon)}f(m)f(m')\,\mathrm{d}m\,\mathrm{d}m' \tag{11}$$

where $u_\mathrm{r}(m,\ m')$ is the relative velocity between bubbles of mass m and bubbles of mass m', and ε_c is the gas volume fraction at compact bubble packing and results in a correction equivalent to the $Y(\varepsilon)$ used by Enskog for dense gases (Ferziger and Kaper, 1972). The highest void fraction that we expect to have in the entire domain is moderate, on the order of 10%, and the correction at this void fraction is on the order of 15%. The effective relative velocity at $\mathbf{r}$ can be calculated as:

$$\mathbf{u}_\mathrm{r}(m,m') = \frac{1}{\pi[R_\mathrm{b}(m)+R_\mathrm{b}(m')]^2}\int_0^{R_\mathrm{b}(m)+R_\mathrm{b}(m')} 2\pi r(\mid\nabla\mid \mathbf{u}_{m'}\mid r+\mid \mathbf{u}_m-\mathbf{u}_{m'}\mid)\mathrm{d}r. \tag{12}$$

Assuming that the bubble velocity gradients are constant in the range of the bubble sizes, we can write the relative velocity as (Williams and Loyalka, 1991):

$$u_\mathrm{r}(m,m') = \frac{4}{3}[R_\mathrm{b}(m)+R_\mathrm{b}(m')]\mid\nabla\mid \mathbf{u}_m\mid+\mid \mathbf{u}_m-\mathbf{u}_{m'}\mid . \tag{13}$$

Following the developments made for the turbulent coalescence kernel in aerosols, we can write, for the contribution of the large scale turbulence, (Williams and Loyalka, 1991):

$$T_{\mathrm{t,l}}(m, m', \mathbf{r}, t) = \left(\frac{3\varepsilon^k}{10\pi v}\right)^{1/2} (v(m)^{1/3} + v(m')^{1/3})^3 f(m) f(m') \tag{14}$$

where ε^k is the dissipation of turbulent kinetic energy k. The small eddies also contribute to the collision rate with a different kernel (Prince and Blanch, 1990):

$$T_{\mathrm{t,s}}(m, m', \mathbf{r}, t) = 1.4\varepsilon^{k^{1/3}} (\mathrm{d}(m) + \mathrm{d}(m'))^2 \mathrm{d}(m)^{1/3} f(m) f(m') \tag{15}$$

where the bubble volume and diameter must be calculated based on the bubble mass and the local conditions.

When the effects of both mean velocity differences and turbulent fluctuations are important, it is usual to superpose both contributions in an algebraic fashion. It is known that this procedure gives reasonable results for low gas volume fractions.

When the gas volume fraction approaches the maximum compactness, ε_{c}, the collision frequency must become infinite as shown in (11), and strong coalescence will occur. For this reason, it is also acceptable to include the compactness correction in (14) and (15) yielding the kernel:

$$T(m, m') = \frac{\varepsilon_{\mathrm{c}}}{(\varepsilon_{\mathrm{c}} - \varepsilon)} [T_{\mathrm{u_r}}(m, m') + T_{t,l}(m, m') + T_{t,\mathrm{s}}(m, m')]. \tag{16}$$

Notice that the average relative velocity can be zero, see (13). Nevertheless, we still can have collisions due to the turbulence kernels and to velocity gradients in each bubble size. It was found in preliminary runs that the contribution of the turbulent terms to the total collision rate was small for the flow under consideration, and thus this effect was not included in the calculations.

The probability that a collision results in a coalescence is usually related to the contact time between the bubbles and to the liquid properties. Prince and Blanch (1990) made a simple model accounting for this term that proved to work well for the case of bubble columns in distilled water. Nevertheless, the modeling of the probability of coalescence is very complex due to the large number of effects that influence the coalescence. On one hand, turbulence and surfactants tend to suppress coalescence, while a close packing of the bubbles at high void fractions increases the probability of coalescence. The model presented by Prince and Blanch (1990) will be used. In this study the probability of coalescence is:

$$\zeta(m, m') = e^{-\frac{t_{m,m'}}{\tau_{m,m'}}} \tag{17}$$

where $t_{m,m'}$ is the time required for coalescence between two bubbles with masses m and m', and $\tau_{m,m'}$ is the contact time between the bubbles. The time required for coalescence is calculated as:

$$t_{m,m'} = C_{\mathrm{s}} \left(\frac{R_{m,m'}^3 \rho_l}{16\sigma}\right)^{1/2} \ln\left(\frac{h_0}{h_{\mathrm{f}}}\right). \tag{18}$$

In (18) h_0 is the initial thickness of the film, about 1×10^{-4} m (Kirkpatrick and Locket, 1974), and h_f is the critical thickness for the film between bubbles for them to break, estimated to be 1×10^{-7} m (Thomas, 1981). $R_{m,m'}$ is the equivalent radius for two bubbles of different radii coalescing and is defined as (Chesters and Hoffman, 1982):

$$R_{m,m'} = 0.5\left(\frac{1}{R_m} + \frac{1}{R_{m'}}\right)^{-1}. \tag{19}$$

In (18) C_s is a constant accounting for the effect of the surfactants. It is known that the presence of surfactants tends to increase the time required for coalescence. In this work a model in which the time required for coalescence increases uniformly for every bubble size will be used. As observed by Prince and Blanch (1990) typical values of C_s can range on the order of $1–10^4$ depending on the surfactant concentration. A reasonable value is 10^3 for the concentrations found in oceanic waters. It is not clear whether C_s depends only on the surfactant concentration or if it should also depend on other variables such as the effective radius. Significantly, C_s, h_0 and h_f have a strong effect on the coalescence rate and only rough estimates are used in this work. Clearly more research is needed in the area of bubble coalescence in the presence of surfactants; nevertheless, the predicted trends should be valid.

The contact time is calculated from the estimate of Levich (1962) of contact time for turbulent flows and the contribution due to relative velocities between the bubbles:

$$\tau_{m,m'} = \frac{2(R_m + R_{m'})^{5/3}}{|\,\mathbf{u}_r(m, m')\,|\,(R_m + R_{m'})^{2/3} + 2(R_m + R_{m'})\varepsilon^{k^{1/3}}} \tag{20}$$

where $\mathbf{u}_r(m, m')$ is the relative velocity between bubbles with masses m and m'.

2.3. Bubble breakup

We consider three breakup mechanisms in this study.

2.3.1. Turbulence induced breakup

The interactions between turbulent liquid eddies and bubbles can cause bubble breakup. Early works on bubble and drop breakup found that there is a critical Weber number of breakup (Hinze, 1955). This results in a critical bubble radius beyond which bubble breakup occurs. The bubble breakup frequency is given by:

$$b_{ti}(m', m - m' \mid m) = 0.055 P_b \varepsilon^{k^{1/3}} d_b(m)^{-2/3} \varphi(m) \delta(m' - m/2) \tag{21}$$

where $\varphi(m)$ is a weighting function, $\delta(m' - m/2)$ is a Dirac's delta function which implies that we will allow the bubbles to split into two identical daughters and P_b is a constant. In the work of Navarro-Valenti et al. (1991) they found that for air/water bubbly flows P_b is 0.155 and $\varphi(m)$ is:

$$\varphi(m) = H(R_b - R_c) \tag{22}$$

where R_c is the critical radius for breakup and H is the Heavyside step function. As explained by Luo and Svendsen (1996), $\varphi(m)$ acts in (21) to avoid unrealistic high breakup rates at small bubbles sizes. It is usually assumed that the bubbles can only be split by eddies which are smaller than the bubble size. In the case of two-phase bubbly flow around a ship, the bubble radii considered are very small compared to the eddy sizes present in the flow, therefore no turbulent breakup is expected. This assumption appears reasonable over all the computational domain except near the propeller and in the boundary layer near the hull, where the turbulent breakup could be very important. No propeller is considered in this work.

2.3.2. Breakup due to velocity gradients

Strong velocity gradients may deform the bubbles causing the breakup. The works made in the subject were reviewed in detail by Clift (1978) and Acrivos (1983). Miksis (1981) found that in axially symmetric shear flows, the critical Weber number for breakup is

$$We_{cr} = \frac{R_b^3 \rho_l G_l^2}{\sigma} = 0.345 \tag{23}$$

where G_l is the local liquid velocity gradient. The critical radius for bubble breakup is thus

$$R_c = \left(\frac{0.345\sigma}{\rho_l G_l^2} \right)^{1/3} \tag{24}$$

or for a given radius we will define the breakup rate in the form:

$$b_s(m', m - m' \mid m) = b_2 \frac{R_b^2(m)}{R_b^2(m) + R_c^2} \delta(m' - m/2). \tag{25}$$

Eq. (25) implies that bubbles smaller than the critical radius tend not to breakup while large bubbles tend to break with equal probability. This model is similar to the one used by Navarro-Valenti et al. (1991). Unfortunately, to our knowledge no theoretical or experimental information is available to estimate the constant b_2. In this work we will assume that the bubbles need to elongate before they break, and that the time required to reach that elongation is proportional to the liquid velocity gradient, so that $b_2 = b_3 G_l$. Here b_3 is assumed to be a constant to be adjusted, and in this work $b = 0.001$ was used. It should be noted that b_3 could be a function of the concentration of surfactants, the turbulence length scale and intensity, etc., but to the knowledge of the authors no information to estimate its value is available. More research is needed on bubble breakup in sea water in order to construct a truly mechanistic model of polydisperse bubbly flows. However, the model used herein is expected to give reasonable results.

At this point a hypothesis must be done to evaluate the size distribution of the daughter bubbles. For the case of turbulent breakup, Luo and Svendsen (1996) provide a model to calculate such a distribution. To the knowledge of the authors, in the case of shear-driven breakup no model nor information is available and we will assume that the bubbles will break into bubbles of half the original mass, as shown in (25).

2.3.3. Tipstreaming (De Bruijn, 1993)

Tipstreaming of bubbles is the ejection of very small bubbles, with radii less than 50 μm (Stone, 1994), from the tip of a deformed bubble in a shear flow. Even though the phenomenon of tipstreaming has been known from the early works of Taylor (1934) and later Rumscheidt and Mason (1961), it was not until recent years that comprehensive and careful experiments have been done on the subject. The conditions observed for the appearance of tipstreaming are mainly a low viscosity ratio, $\lambda = \mu_g/\mu_l < 0.1$ (λ is about 0.02 for air bubbles in water) and the presence of surfactants. These two conditions are met in the case of bubbles in the ocean, and the velocity gradients near the hull of a ship can be strong enough to cause tipstreaming. Therefore, the potential effect of this phenomenon on the bubble size distribution was studied. A breakup kernel similar to that of point the second mechanism was used, even though some tipstreaming experiments evidence a smaller critical radius than that observed for normal breakup (Stone, 1994). To estimate the breakup rate (25) was used and it was arbitrarily assumed that the tipstreaming bubbles were separated by about 10 times the radius of the mother bubble, resulting in:

$$b_t(m', m - m' \mid m) = \frac{G_l}{10} \frac{R_b^2(m)}{R_b^2(m) + r_c^2} \delta[R_b(m') - R_b(m)] \tag{26}$$

where the radius of the ejected bubbles (corresponding to m') was assumed to be 20 or 30 μm with the same probability. Additionally, as very small bubbles do not break, bubbles with volumes smaller than six times the volume of the ejected bubbles were not allowed to tipstream. This results in three bubbles for each tipstreaming event, the mother bubble plus two tipstream small bubbles.

In general, as in the case of coalescence, the different mechanisms contributing to the breakup probability are added linearly. Nonlinear effects, such as the breakup produced by a turbulent eddy hitting a deformed bubble in a shear flow, are expected to be less important and are neglected.

Clearly, more research is needed to better quantify this phenomenon, nevertheless, as before, the parametric trends given in this study should be realistic.

2.4. Gas dissolution

The bubbles can change their mass if condensation or evaporation occurs, if they coalesce or breakup, or if gas is lost or gained due to mass diffusion. If, in the last case, the gas is lost we call this term dissolution. The gas diffusion into or out of a bubble can be written as (Levich, 1962; Smith and Hyman, 1987):

$$\frac{dm}{dt} = 8(C_\infty - C_0)\kappa^{2/3} \mid \mathbf{u}_r \mid^{1/3} R_b^{4/3} \tag{27}$$

where C_∞ and C_0 are the gas concentrations very far away and at the bubble surface, respectively, κ is the diffusivity of air in water (2×10^{-9} m^2/s), $\mathbf{u}_r$ is the relative velocity between the bubble and the liquid and R_b is the bubble radius.

The gas concentrations are approximated using the relations:

$$C_0 = H\left(p_{\text{atm}} - \rho_l g z + \frac{2\sigma}{R_b} + p\right), \tag{28}$$

$$C_\infty = H p_{\text{atm}} \tag{29}$$

where H is the Henry constant (0.000238 g/Nm) and p is the piezometric pressure.

Notice that, due to the presence of the piezometric pressure in (28), it is possible to have bubble growth in regions of low pressure. This could happen in the stern region near the surface or near the propeller. This causes aeration at the propeller that could be responsible for a significant amount of air entrainment in the flow.

2.5. Multigroup approach

The numerical solution of (7) can be accomplished using a multigroup scheme, assuming that all the bubbles of mass between $m_{g-1/2}$ and $m_{g+1/2}$ can be represented in a group-g by a single bubble mass, m_g. We note that $m_{g-1/2}$ and $m_{g+1/2}$ must be chosen using some adequate criteria, such as good representation of the distribution, computational advantage, etc. Integrating (7) between $m_{g-1/2}$ and $m_{g+1/2}$ one obtains:

$$\frac{\partial N_g}{\partial t} + \frac{\partial j^N_{g,j}}{\partial x_j} + \left[\frac{\mathrm{d}m}{\mathrm{d}t} f(m, \mathbf{r}, t)\right]_{m_{g-1/2}}^{m_{g+1/2}} = \int_{m_{g-1/2}}^{m_{g+1/2}} \left[\beta(m, \mathbf{r}, t) + \chi(m, \mathbf{r}, t) + S(m, \mathbf{r}, t)\right] \mathrm{d}m \tag{30}$$

where the bubble flux in the group-g can be calculated as

$$J^N_{g,j} = \int_{m_{g-1/2}}^{m_{g+1/2}} u_{g,j}(m, \mathbf{r}, t) f(m, \mathbf{r}, t)\, \mathrm{d}m \tag{31}$$

and the group number density is defined as

$$N_g(\mathbf{r}, t) = \int_{m_{g-1/2}}^{m_{g+1/2}} f(m, \mathbf{r}, t)\, \mathrm{d}m. \tag{32}$$

As a further assumption, the distribution function, the bubble velocities, the bubble mass exchange rate and the breakup and coalescence probability are assumed constant in each group. Additionally, an upwinding approach is used to calculate the mass loss (or gain) rate in (30). Under these conditions (30) can be simplified to:

$$\begin{aligned}\frac{\partial N_g}{\partial t} + \frac{\partial (u_{g,j} N_g)}{\partial x_j} &= \beta_g^+ - \beta_g^- + \chi_g^+ - \chi_g^- + S_g \\ &- \frac{1}{m_{g+1} - m_g}\left[\min\left(\frac{\mathrm{d}m}{\mathrm{d}t}, 0\right) N(\mathbf{r}, t)\right]_{g+1} + \frac{1}{m_g - m_{g-1}}\left[\min\left(\frac{\mathrm{d}m}{\mathrm{d}t}, 0\right) N(\mathbf{r}, t)\right]_g \\ &- \frac{1}{m_{g+1} - m_g}\left[\max\left(\frac{\mathrm{d}m}{\mathrm{d}t}, 0\right) N(\mathbf{r}, t)\right]_g + \frac{1}{m_g - m_{g-1}}\left[\max\left(\frac{\mathrm{d}m}{\mathrm{d}t}, 0\right) N(\mathbf{r}, t)\right]_{g-1}.\end{aligned} \tag{33}$$

The mass change rate in a bubble, dm/dt, is negative for the case of condensation or gas dissolution, and is positive in the case of evaporation or gas diffusion into the bubble. The bubble breakup, coalescence and volume sources and losses are also integrated over each group, resulting in the terms on the right hand side of (33). The calculation of these terms requires the precise determination of the mass of each group. Typically two cases are possible:

1. The group masses are determined by the constant lower and upper limit masses which are assumed to be

$$\{m_{1-1/2}, m_{1+1/2}, \ldots, m_{g-1/2}, m_{gi+1/2}, \ldots, m_{NG+1/2}\} \tag{34}$$

where NG is the total number of groups, and the average mass for each group is:

$$\{m_1, m_2, \ldots, m_g, \ldots, m_{NG}\}. \tag{35}$$

As an example, if the maximum and minimum bubble sizes in the distribution can be estimated, the groups will be chosen so as to cover all the possible relevant masses. Additionally, computational advantages can arise if the mass difference between the groups is constant. It is known that this approach can cause numerical diffusion in the probability distribution function when the mass exchange rate is large (Williams and Loyalka, 1991), however the method has been shown to be robust.

2. The group masses are variable and dependent on the position and time, in order to follow the characteristic lines of the bubbles. In this case, there is no transfer between the groups due to the mass exchange rate, but the evaluation of the coalescence and breakup terms is considerably more complicated (Williams and Loyalka, 1991). If no breakup or coalescence occurs and the group mass is chosen such that the mass exchange rate term is zero (33) simplifies to:

$$\frac{\partial N_g}{\partial t} + \frac{\partial (u_{g,j} N_g)}{\partial x_j} = 0. \tag{36}$$

The formulation (2) of the multigroup scheme has the important advantage of low numerical diffusion in the intergroup mass transfer. The main disadvantages are restriction to the case with no or small bubble breakup or coalescence and the need for an additional equation for mass conservation within each group in order to determine bubble volume:

$$\frac{\partial (\rho_g \varepsilon_g)}{\partial t} + \frac{\partial (u_{g,j} \rho_g \varepsilon_g)}{\partial x_j} = \frac{dm}{dt} N_g. \tag{37}$$

The bubble volume (necessary for the determination of the bubble mass change rate and drag coefficient) can be calculated from the relationship between the bubble number density and the volume fraction in group-g:

$$v_{b,g} = \frac{\varepsilon_g}{N_g}. \tag{38}$$

Approach (2) was used by Carrica et al. (1997) to obtain results for monodisperse two-phase flow around a ship with bubble dissolution.

In the rest of this paper we will restrict ourselves to method (1), constant mass in each group. In this case the bubble volume fraction is related to the group number density by:

$$\varepsilon(\mathbf{r}, t) = \sum_{g=1}^{NG} \frac{m_g N_g(\mathbf{r}, t)}{\rho_g(\mathbf{r}, t)}. \tag{39}$$

This multigroup model can be solved in combination with a two-fluid model to calculate the gas velocity field for each group. The standard monodisperse two-fluid model with no source can be recovered assuming that the bubble size distribution is single-valued at each position and therefore the dissolution, breakup and coalescence terms are zero. Under these conditions (33) reduces to:

$$\frac{\partial N}{\partial t} + \frac{\partial (u_j N)}{\partial x_j} = 0 \tag{40}$$

and the continuity equation is obtained by multiplying by the bubble mass

$$\frac{\partial (\rho_g \varepsilon)}{\partial t} + \frac{\partial (\rho_g \varepsilon u_j)}{\partial x_j} = 0. \tag{41}$$

2.6. Two-fluid model

The multigroup two-fluid model is derived based on the single group two-fluid model developed over the years at RPI (Drew and Lahey, 1979; Arnold, 1988; Park, 1922; Alajbegovic, 1994) and by others (Delhaye, 1981; Ishii, 1975). Eq. (33) will be solved along with the momentum equations for the liquid and gaseous phases and the continuity equation for the liquid arising from the two-fluid model. The three dimensional two-fluid model can be written as:

$$\frac{\partial \varepsilon_k \rho_k}{\partial t} + \frac{\partial}{\partial x_j}(\varepsilon_k \rho_k u_{k,j}) = S_k, \tag{42}$$

$$\frac{\partial \varepsilon_k \rho_k u_{k,i}}{\partial t} + \frac{\partial}{\partial x_j}(\varepsilon_k \rho_k u_{k,i} u_{k,j}) = \frac{\partial}{\partial x_j}[\varepsilon_k(\tau_{k,ij} + \tau_{k,ij}^{Re})] + M_{k,i} - \varepsilon_k \rho_k g \delta_{i3} \tag{43}$$

where $k = g$ or l denotes the gas group-g or the liquid phase, ε_k is the phasic volume fraction at liquid or group-g, ρ_k is the phasic density, $u_{k,i}$ is the velocity of phase-k, $\tau_{k,ij}$ and $\tau_{k,ij}^{Re}$ are the viscous stress tensor and the turbulent stress tensor of phase-k, $M_{k,i}$ is the interfacial momentum transfer between the phases, and the last term on the right hand side of (2) is the gravitational force.

We have included a mass source S_k in (42). In this work this global source is exclusively due to gas dissolution into the liquid, which could be positive or negative. Since this process is very slow, its effect on the momentum transfer between the phases is negligible. In addition, due to the relatively small gas volume and density, this mass source is negligible for the liquid phase.

Consequently, the liquid continuity equation reduces to:

$$\frac{\partial(\varepsilon_l\rho_l)}{\partial t}+\frac{\partial}{\partial x_j}(\varepsilon_l\rho_l u_{l,j})=0 \tag{44}$$

where the liquid density, ρ_l, is considered to be constant.

Assuming that the inertia and shear stress tensors are negligible for the gas phase, we can write the gas momentum equation for the group-g ($g = 1, 2, \ldots, NG$) as

$$-\frac{\partial}{\partial x_i}(\varepsilon_g p)+\varepsilon_g\rho_g g\delta_{i3}+M_{g,i}=0 \tag{45}$$

where the interfacial momentum transfer term for the liquid phase can be written as

$$M_{l,i}=-\sum_{g=1}^{NG}M_{g,i}. \tag{46}$$

Expanding the interfacial exchange terms we can write the gas momentum equation for group-g in the form (Carrica et al., 1997):

$$-\frac{\partial(\varepsilon_g p)}{\partial x_i}-\varepsilon_g\rho_g g\delta_{i3}-p\frac{\partial(1-\varepsilon)}{\partial x_i}+M_{g,i}^{VM}+M_{g,i}^{L}+M_{g,i}^{D}+M_{g,i}^{TD}=0 \tag{47}$$

where the source was separated into the virtual mass, lift, drag and turbulent dispersion force contributions. The virtual mass term accounts for the effect of the acceleration of the liquid surrounding the bubbles and is usually modeled as (Drew and Lahey, 1979):

$$M_{g,i}^{vm}=\varepsilon_g\rho_l C_{vm}\left[\left(\frac{\partial u_{l,i}}{\partial t}+u_{l,j}\frac{\partial u_{l,i}}{\partial x_j}\right)-\left(\frac{\partial u_{g,i}}{\partial t}+u_{g,j}\frac{\partial u_{g,i}}{\partial x_j}\right)\right]. \tag{48}$$

The virtual mass coefficient, C_{vm}, assumed to be 0.5, the value obtained for a spherical bubble in dilute potential flow (Lahey and Drew, 1990).

In the two-fluid model, the lift force term is modeled after ensemble averaging forces on a bubble immersed in a shear flow, and can be expressed as (Drew and Lahey, 1987; Drew and Lahey, 1990):

$$M_{g,i}^{\mathrm{L}}=-\varepsilon_g\rho_l C_{\mathrm{L}}\varepsilon_{ijk}\varepsilon_{klm}(u_{l,j}-u_{g,j})\frac{\partial u_{l,l}}{\partial x_m}. \tag{49}$$

In (49) ε_{ijk} is the third order permutation tensor and C_{L} is the lift coefficient, which has been found to be about 0.1 for most practical two-phase air/water flows (Wang et al., 1987).

The drag force may be expressed as:

$$M_{g,i}^{\mathrm{D}}=\varepsilon_g\rho_l\frac{3}{8}\frac{C_{\mathrm{D}}}{R_g}(u_{l,i}-u_{g,i})\mid\mathbf{u}_{g,r}\mid \tag{50}$$

where C_{D} is the drag coefficient, which, including void fraction effects, is given by (Ishii, 1987)

$$C_{\mathrm{D}}=\frac{12}{Re_g(1-\varepsilon_l)}(1+0.168Re_g^{0.75}) \tag{51}$$

where Re_g is the bubble Reynolds number based on the bubble radius at group-g, R_g, and the magnitude of the gas/liquid relative velocity at group-g, $\mathbf{u}_{g,r}$. Eq. (51) reduces to the Stokes drag coefficient when the bubble Reynolds number is small and the gas volume fraction is negligible.

The turbulent dispersion term is modeled as (Carrica et al., 1997):

$$M_{g,i}^{\mathrm{TD}} = -\rho_l \frac{\varepsilon_g}{N_g} \frac{3}{8} \frac{C_{\mathrm{D}} \mid \mathbf{u}_{g,r} \mid}{R_g} \frac{v_t}{Sc_{\mathrm{b}}} \frac{\partial N_g}{\partial x_i} \tag{52}$$

where Sc_{b} is the bubble Schmidt number

$$Sc_{\mathrm{b}} = \frac{v_t}{v_{\mathrm{b}}} \tag{53}$$

and v_{b} is the bubble diffusivity. Some experimental evidence (Loth and DeAngelis, 1996) shows that Sc_{b} is between 0.7 and 1.0 for small particles. As no further information is available, in this work we assume that the Schmidt number is 1. The effect of different turbulent dispersion coefficients in monodisperse bubbly flow around a ship has been studied in Paterson et al. (1996).

Using (43), (45) and (46) we can write the two-phase modified RANS liquid momentum equation as

$$\begin{aligned} &\frac{\partial u_{l,i}}{\partial t} + U_{l,j} \frac{\partial u_{l,i}}{\partial x_j} + \frac{1}{\varepsilon_l} \frac{\partial}{\partial x_j} [\varepsilon_l \overline{u'_{l,i} u'_{l,j}}] = \\ &\quad -\frac{1}{\rho_l} \frac{\partial p}{\partial x_i} + \frac{v}{\varepsilon_l} \frac{\partial}{\partial x_j} \left[\varepsilon_l \left(\frac{\partial u_{l,i}}{\partial x_j} + \frac{\partial u_{l,j}}{\partial x_i} \right) \right] + \frac{\varepsilon_l \rho_l + (1-\varepsilon_l)\rho_g}{\varepsilon_l \rho_l} g \delta_{i3} \end{aligned} \tag{54}$$

where the third term on the left hand side is the Reynolds stress tensor, and is constituted as

$$-\overline{u'_{l,i} u'_{l,j}} = v_t \left(\frac{\partial u_{l,i}}{\partial x_j} + \frac{\partial u_{l,j}}{\partial x_i} \right) - \frac{2}{3} \delta_{ij} k \tag{55}$$

and $k = 1/2\ (\overline{\mathrm{u}'_{l,i}\mathrm{u}'_{l,\mathrm{j}}})$ is the liquid turbulent kinetic energy.

2.7. Turbulence model

The Baldwin–Lomax model (Baldwin and Lomax, 1978) was used to calculate the turbulent quantities for the liquid. In this algebraic model, the turbulent viscosity close to the wall and the outer layer are calculated as:

$$v_{tl,w} = \ell_m^2 \mid \bar{\omega} \mid, \tag{56}$$

$$v_{tl,o} = C_k C_{\mathrm{cp}} F_{\mathrm{wk}} F_{\mathrm{Kleb}} \tag{57}$$

where ℓ_m is the mixing length, $\bar{\omega}$ is the vorticity, F_{wk} is the wake function, F_{Kleb} is the Klebanoff intermittence function, and C_k and C_{cp} are empirical constants of the model.

The characteristic length, ℓ_m, is calculated in the near hull region as:

$$\ell_m = \kappa y\left[1 - \exp\left(-\frac{y^+}{A^+}\right)\right] \tag{58}$$

where y is the distance to the wall and y^+ is its dimensionless form using the friction velocity. For the bubble-induced turbulence, the model of Sato (1981) was used. In this model, bubble-induced turbulence results in an additional turbulent viscosity as:

$$\nu_{\mathrm{tb}} = \sum_{g=1}^{NG} 1.2 R_g \varepsilon_g \mid \mathbf{u}_{g,r} \mid \tag{59}$$

wherein 1.2 R_g (group radius) is the characteristic length and the group relative velocity $\mathbf{u}_{g,r}$ is the characteristic velocity. Additionally, the total viscosity is calculated using linear superposition (Lance and Bataille, 1991):

$$\nu_{\mathrm{eff}} = \nu + \nu_t = \nu + \nu_{tl} + \nu_{tb}. \tag{60}$$

The liquid turbulent kinetic energy is not computed directly from this turbulence model, but can be calculated assuming the following relationship between the mixing length and the eddy viscosity of the k–ε model:

$$k_{1\phi} = \left(\frac{C_\ell \nu_{tl}}{C_\mu \ell_m}\right)^2 \tag{61}$$

where $C_\ell = 0.4$ and $C_\mu = 0.09$ are constants in the k–ε model. The characteristic length, ℓ_m, is calculated in the near hull region with (58), and the outer region and wake are assumed to be:

$$\ell_m = F_{\mathrm{wk}} = \min\left(y_{\max} F_{\max}, C_{\mathrm{wk}} y_{\max} \frac{u_{\mathrm{diff}}^2}{F_{\max}}\right)/u_{\mathrm{diff}} \tag{62}$$

where u_{diff} is the maximum difference in liquid velocities in a plane (y–z) perpendicular to the axis of the ship.

The turbulent kinetic energy was also modified to account for the effect of the bubbles. The same linear superposition principle was applied for the bubble-induced kinetic energy yielding (Lance and Bataille, 1991):

$$k = k_{1\phi} + k_{\mathrm{b}} \tag{63}$$

where k_{b} is the turbulent kinetic energy induced by the bubbles and $k_{1\phi}$ is the single-phase turbulent kinetic energy, calculated from (61). This model may be considered valid for local void fractions up to about 3%. For higher values, interactions between the bubbles may increase the bubble-induced turbulent kinetic energy. The bubble-induced turbulence results in an additional pseudo-turbulent kinetic energy as an extension of the single size form (Sato and Sadatomi, 1981)

$$k_{\mathrm{b}} = C_{\mathrm{p}} \sum_{g=1}^{NG} \varepsilon_g (1 - \varepsilon_g) \mid \mathbf{u}_{g,r} \mid^2 \tag{64}$$

and the dissipation of turbulent kinetic energy can be estimated by:

$$\varepsilon^k = 0.09 \frac{k^2}{\nu_t}. \tag{65}$$

2.8. Dimensionless equations

Nondimensionalizing the equations using a characteristic length L and velocity U_0 (length and velocity of the ship) and the gas density at normal pressure, and using the interfacial momentum transfer terms, (48)–(52), (33), (44), (47) and (54) yield the final system of equations to be solved.

2.8.1. *Bubble group-g* number density equation

$$\frac{\partial \hat{N}_g}{\partial \hat{t}} + \frac{\partial (\hat{u}_{g,j} \hat{N}_g)}{\partial \hat{x}_j} + \frac{1}{\hat{m}_{g+1} - \hat{m}_g} \left[\min\left(\frac{\mathrm{d}\hat{m}}{\mathrm{d}\hat{t}}, 0 \right) \hat{N} \right]_{g+1} - \frac{1}{\hat{m}_g - \hat{m}_{g-1}} \left[\min\left(\frac{\mathrm{d}\hat{m}}{\mathrm{d}\hat{t}}, 0 \right) \hat{N} \right]_{g} +$$

$$\frac{1}{\hat{m}_{g+1} - \hat{m}_g} \left[\max\left(\frac{\mathrm{d}\hat{m}}{\mathrm{d}\hat{t}}, 0 \right) \hat{N} \right]_{g} - \frac{1}{\hat{m}_g - \hat{m}_{g-1}} \left[\max\left(\frac{\mathrm{d}\hat{m}}{\mathrm{d}\hat{t}}, 0 \right) \hat{N} \right]_{g-1}$$

$$= \hat{\beta}_g^+ - \hat{\beta}_g^- + \hat{\chi}_g^+ - \hat{\chi}_g^-. \tag{66}$$

2.8.2. *Liquid continuity equation*

$$\frac{\partial \varepsilon_l}{\partial \hat{t}} + \frac{\partial [\varepsilon_l \hat{u}_{l,j}]}{\partial \hat{x}_j} = 0. \tag{67}$$

2.8.3. *Liquid momentum equations*

$$\frac{\partial \hat{u}_{l,i}}{\partial \hat{t}} + \left[\hat{u}_{l,j} - \frac{1}{\varepsilon_l} \frac{\partial}{\partial \hat{x}_j} \left(\frac{\varepsilon_l}{Re_t} \right) \right] \frac{\partial \hat{u}_{l,i}}{\partial \hat{x}_j} - \frac{1}{\varepsilon_l} \frac{\partial}{\partial \hat{x}_j} \left(\frac{\varepsilon_l}{Re_t} \right) \frac{\partial \hat{u}_{l,j}}{\partial \hat{x}_i} =$$

$$- \frac{\partial}{\partial \hat{x}_i} \left(\hat{p} + \frac{2}{3} \hat{k} \right) + \frac{1}{Re_t} \frac{\partial}{\partial \hat{x}_j} \left(\frac{\partial \hat{u}_{l,i}}{\partial \hat{x}_j} + \frac{\partial \hat{u}_{l,j}}{\partial \hat{x}_i} \right) + \frac{1 - \varepsilon_l}{\varepsilon_l} \left[- \frac{\partial}{\partial \hat{x}_i} \left(\hat{p} + \frac{2}{3} \hat{k} \right) + \frac{1}{Fr^2} \right]. \tag{68}$$

2.8.4. Gas group-g momentum equations

$$C_{vm}\left[\left(\frac{\partial \hat{u}_{g,i}}{\partial \hat{t}}+\hat{u}_{g,j}\frac{\partial \hat{u}_{g,i}}{\partial \hat{x}_j}\right)-\left(\frac{\partial \hat{u}_{l,i}}{\partial \hat{t}}+\hat{u}_{l,j}\frac{\partial \hat{u}_{l,i}}{\partial \hat{x}_j}\right)\right]=-C_{\mathrm{L}}\varepsilon_{ijk}\varepsilon_{klm}(\hat{u}_{l,j}-\hat{u}_{g,j})\frac{\partial \hat{u}_{l,l}}{\partial \hat{x}_m}$$
$$+\hat{C}_{\mathrm{D}}(\hat{u}_{l,i}-\hat{u}_{g,i})\mid \mathbf{u}_r\mid -\frac{\partial}{\partial \hat{x}_l}\left(\hat{p}+\frac{2}{3}\hat{k}\right)+\frac{\delta_{i,3}}{Fr^2}-\hat{C}_{\mathrm{D}}\mid u_r\mid \frac{\hat{\nu}_t}{Sc_{\mathrm{b}}}\frac{1}{\hat{N}_g}\frac{\partial \hat{N}_g}{\partial \hat{x}_i} \tag{69}$$

where the resulting dimensionless parameters are the Reynolds and Froude numbers and the modified drag coefficient:

$$Re_{\mathrm{t}}=\frac{U_0 L}{\nu_{\mathrm{eff}}},\quad Fr=\frac{U_0}{\sqrt{gL}},\quad \hat{C}_{\mathrm{D}}=\frac{3}{8}C_{\mathrm{D}}\frac{L}{R_{\mathrm{b}}}. \tag{70}$$

From this point on, the cap for the dimensionless variables will be omitted for simplicity.

3. Numerical method

3.1. Intergroup transfer

The numerical implementation of the coalescence terms χ^+ and χ^- is rather complex and requires a model for the mass transfer between the groups. With the assumptions made for the multigroup model we can define a group collision kernel as:

$$\int_{m_l}\int_{m_k}\zeta(m,m')T(m,m')\,\mathrm{d}m\,\mathrm{d}m'=C_{kl}T_{kl}N_kN_l. \tag{71}$$

The coalescence source can be then calculated as:

$$C_g^+=\frac{1}{2}\sum_{k\le g}C_{kl}T_{kl}\mathbf{X}_{gkl}N_kN_l \tag{72}$$

where l is such that $m_{g-1}<m_k+m_l<m_{g+1}$ and $\mathbf{X}_{gkl}$ is a matrix with components having a value between 0 and 1 that accounts for the amount of gas that is transferred from the coalescence of two bubbles from groups k and l to the group-g

$$\mathbf{X}_{gkl}=\frac{m_k+m_l-m_{g-1}}{m_g-m_{g-1}}(m_k+m_l<m_g),$$
$$\mathbf{X}_{gkl}=\frac{m_k+m_l-m_{g+1}}{m_g-m_{g+1}}(m_k+m_l>m_g). \tag{73}$$

If the group masses are chosen such as the mass interval is constant, the matrix $\mathbf{X}_{gkl}$ will be filled with 1 and 0, because the sum of the masses of any two groups will be coincident with the mass of other groups. However, if the group masses are chosen with non constant intervals

in mass, the daughter bubble will generally not have a mass coincident with one of the group masses. In this model the gas is transferred to the two nearest groups to the sum of the masses k and l using a linear distribution. This implies that the total mass $m_k + m_l$ will be distributed linearly between the groups g and $g + 1$, or between the groups $g-1$ and g.

On the same grounds, the losses due to coalescence can be calculated as:

$$C_g^- = \sum_{k=1}^{NG} C_{gk} T_{gk} N_g N_k. \tag{74}$$

For the breakup sources, the procedure is similar. After integration of (9) we can write the bubble breakup source terms for group-g as:

$$\beta_g^+ = \sum_{k=g}^{NG} b_k N_k \mathbf{X}_{gk} \tag{75}$$

where b_k is the total breakup rate evaluated at the mass of the group-k. The matrix $\mathbf{X}_{gk}$ is defined using the same assumptions as in the case of the mass conservation matrix $\mathbf{X}_{gkl}$ for the coalescence case, thus resulting in a mass conservation matrix of the form:

$$\begin{aligned}
\mathbf{X}_{gk} &= 2\frac{m_k/2 - m_{g-1}}{m_g - m_{g-1}} (m_{g-1} < m_k/2 < m_g), \\
\mathbf{X}_{gk} &= 2\frac{m_k/2 - m_{g+1}}{m_g - m_{g+1}} (m_{g+1} > m_k/2 > m_g), \\
\mathbf{X}_{gk} &= 0 \quad \text{otherwise}
\end{aligned} \tag{76}$$

and the sink terms are calculated as

$$\beta_g^- = b_g N_g. \tag{77}$$

In the multigroup implementation, the bubbles of the minimum size group that were dissolving were considered lost. Additionally, no breakup was allowed in this group, which is reasonable if it has a very small bubble size. In the case of a coalescence event of any bubble with a bubble in the last group, the mass was conserved in the event incrementing accordingly the number density in the last group, because no bigger bubbles than the largest group were allowed.

3.2. Coordinate transformation

In order to accommodate the complex geometry of the hull of the ship, the equations were transformed from the physical domain with Cartesian coordinates (x, y, z) into the computational domain with curvilinear coordinates (ξ, η, ζ). Following Stern et al. (1996), the transformation was chosen such that in the computational domain, the computational cells are cubic with sides of unity length. The transformation relations for an arbitrary scalar ϕ and

vector **u** in conservative form are (Thompson, 1982)

$$\nabla \cdot \mathbf{u} = \frac{1}{\mathrm{J}} \frac{\partial}{\partial \xi_j} (b^j_i u_i), \tag{78}$$

$$\nabla \phi|_i = \frac{1}{\mathrm{J}} b^j_i \frac{\partial \phi}{\partial \xi_j}, \tag{79}$$

$$\nabla^2 \phi = g_{ij} \frac{\partial^2 \phi}{\partial \xi_i \partial \xi_i} + f_i \frac{\partial \phi}{\partial \xi_i}, \tag{80}$$

$$\frac{\partial \phi}{\partial l} = \frac{\partial \phi}{\partial \tau} - \frac{1}{\mathrm{J}} b^j_i \frac{\partial x_i}{\partial \tau} \frac{\partial \phi}{\partial \xi_j} \tag{81}$$

and the Jacobian of the transformation and the geometrical coefficients are calculated as

$$b^j_l = \varepsilon_{lmn} \frac{\partial x_m \partial x_n}{\partial \xi_j \partial \xi_k} \tag{82}$$

$$g_{ij} = \frac{1}{\mathrm{J}^2} b^i_m b^j_m, \tag{83}$$

$$f_i = \frac{1}{\mathrm{J}} \frac{\partial}{\partial \xi_j} (\mathrm{J} g_{ij}), \tag{84}$$

$$\mathrm{J} = \begin{vmatrix} x_\xi & x_\eta & x_\zeta \\ y_\xi & y_\eta & y_\zeta \\ z_\xi & z_\eta & z_\zeta \end{vmatrix} \tag{85}$$

where the contravariant and modified contravariant velocities for a velocity vector $\mathbf{u} = (U, V, W)$ are defined as

$$\breve{U}_i = \frac{1}{\mathrm{J}} b^i_j u_j = \frac{1}{\mathrm{J}} (b^i_1 U + b^i_2 V + b^i_3 W) \tag{86}$$

$$\hat{U}_i = b^i_j u_j = (b^i_1 U + b^i_2 V + b^i_3 W). \tag{87}$$

Eqs. (66)–(69) were transformed using the transformation relations (78)–(81) yielding the final set of equations.

3.2.1. Liquid continuity equation

$$\frac{\partial (1-\varepsilon)}{\partial \tau} + \frac{1}{\mathrm{J}} \frac{\partial [(1-\varepsilon) \hat{U}_{l,j}]}{\partial \xi_j} = \frac{1}{\mathrm{J}} b^j_i \frac{\partial x_i}{\partial \tau} \frac{\partial (1-\varepsilon)}{\partial \xi_j}. \tag{88}$$

3.2.2. Liquid momentum equation

$$\frac{\partial u_{l,j}}{\partial \tau} - \frac{b_i^j}{\mathrm{J}}\frac{\partial x_i}{\partial \tau}\frac{\partial u_{l,j}}{\partial \xi_j} + \frac{b_n^j}{\mathrm{J}}\left(u_{l,n} - \frac{\partial x_n}{\partial \tau} - \frac{1}{(1-\varepsilon)}\frac{b_n^m}{\mathrm{J}}\frac{\partial[(1-\varepsilon)/Re]}{\partial \xi_m}\right)\frac{\partial u_{l,i}}{\partial \xi_j}$$
$$- \frac{1}{(1-\varepsilon)}\frac{b_j^m}{\mathrm{J}}\frac{b_i^n}{\mathrm{J}}\frac{\partial[(1-\varepsilon)/Re_t]}{\partial \xi_m}\frac{\partial u_{l,j}}{\partial \xi_n} = -\frac{b_i^j}{\mathrm{J}}\frac{\partial}{\partial \xi_j}\left(p + \frac{2}{3}k\right) + \frac{1}{Re_t}g_{kj}\frac{\partial^2 u_{l,i}}{\partial \xi_k \partial \xi_j}$$
$$+ f_j\frac{\partial u_{l,i}}{\partial \xi_j} + \frac{1}{Re_t}\frac{b_i^k}{\mathrm{J}^2}\frac{\partial^2 \hat{U}_{l,j}}{\partial \xi_k \partial \xi_j} - \frac{\varepsilon}{1-\varepsilon}\left[-\frac{b_i^j}{\mathrm{J}}\frac{\partial}{\partial \xi_j}\left(p + \frac{2}{3}k\right) + \frac{\partial_{i3}}{Fr^2}\right]. \tag{89}$$

3.2.3. Gas group-g number density equation

$$\frac{\partial N_g}{\partial \tau} + \frac{1}{\mathrm{J}}\frac{\partial(\hat{U}_{g,j}\hat{N}_g)}{\partial \xi_j} = \frac{1}{\mathrm{J}}b_i^j\frac{\partial x_i}{\partial \tau}\frac{\partial N_g}{\partial \xi_j} + \beta_g^+ - \beta_g^- + \chi_g^+ - \chi_g^-$$
$$- \frac{1}{m_{g+1} - m_g}\left[\min\left(\frac{\mathrm{d}m}{\mathrm{d}t}, 0\right)N\right]_{g+1} + \frac{1}{m_g - m_{g-1}}\left[\min\left(\frac{\mathrm{d}m}{\mathrm{d}t}, 0\right)\hat{N}\right]_g$$
$$- \frac{1}{m_{g+1} - m_g}\left[\max\left(\frac{\mathrm{d}m}{\mathrm{d}t}, 0\right)N\right]_g + \frac{1}{m_g - m_{g-1}}\left[\max\left(\frac{\mathrm{d}m}{\mathrm{d}t}, 0\right)N\right]_{g-1}. \tag{90}$$

3.2.4. Gas group-g momentum equation

$$C_{vm}\left(\frac{\partial u_{g,i}}{\partial \tau} - \frac{b_i^j}{\mathrm{J}}\frac{\partial x_i}{\partial \tau}\frac{\partial u_{g,i}}{\partial \xi j} - \breve{U}_{g,j}\frac{\partial u_{g,i}}{\partial \xi_j}\right)$$
$$= C_{vm}\left(\frac{\partial u_{l,i}}{\partial \tau} - \frac{b_i^j}{\mathrm{J}}\frac{\partial x_i}{\partial \tau}\frac{\partial u_{g,i}}{\partial \xi_j} + \breve{U}_{l,j}\frac{\partial u_{l,i}}{\partial \xi_j}\right) - C_{\mathrm{L}}\varepsilon_{ijk}\varepsilon_{klm}(u_{l,j} - u_{g,j})\frac{b_m^n}{\mathrm{J}}\frac{\partial u_{l,l}}{\partial \xi_n} \tag{91}$$
$$+ \hat{C}_{\mathrm{D}}(u_{l,i} - u_{g,i}) \mid \mathbf{u}_r \mid + \frac{\delta_{i,3}}{Fr_{\mathrm{b}}^2} - \frac{b_i^j}{\mathrm{J}}\frac{\partial}{\partial \xi_j}\left(p + \frac{2}{3}k\right) - \frac{1}{N_g}\hat{C}_{\mathrm{D}} \mid u_{\mathrm{r}} \mid \frac{\hat{\nu}_t + \hat{\nu}_{\mathrm{b}}}{Sc_{\mathrm{b}}}\frac{b_i^j}{\mathrm{J}}\frac{\partial N_g}{\partial \xi_j}.$$

It should be noted that, in the case we study in this paper, the terms due to the temporal variation of the grid are zero because we assume no surface deflection. Then the shape of the free surface, and consequently the grid, are not changing with time.

3.3. Solution method

The gas phase conservation equations were solved using a control-volume upwinding approach (Patankar, 1980). Even though the full upwinding method is only first order accurate, a more complex method is not necessary for the gas momentum equations because

the equations are source-dominated and, if not for the virtual mass term, the equations would be algebraic.

For the group number density equations a TVD flux limiter was added to reduce the artificial numerical diffusivity (Roe, 1985; Sweby, 1985). The resulting scheme is second-order accurate in 1-D advection problems and has proved to successfully reduce the numerical diffusion avoiding spurious oscillations in hyperbolic problems in two or three dimensions (Tamamidis and Assanis, 1993; Saxena and Ravi, 1995).

A control volume in the computational domain has unit length on each side and the convention used to denote the neighboring nodes is N, S, E, W, D and U for north, south, east, west, down and up, respectively. The properties at the faces of the control volume are calculated by linear interpolation and are represented with lower case letters. The group-g number density Eq. (90) are integrated using a simple first order implicit formulation for the time derivative. This results in the following scheme:

$$\begin{aligned}\frac{N_{g,P}-N_{g,P}^{n-1}}{\Delta\tau} =& \max(\hat{V}w,0)[N_{g,W}+C_o\varphi(r_w^-)\Delta N_{g,w}^-]+\min(\hat{V}_w,0)[N_{g,P}-C_o\varphi(r_w^+)\Delta N_{g,w}^+]\\ &-\max(\hat{V}_e,0)[N_{g,P}+C_o\varphi(r_e^-)\Delta N_{g,e}^-]-\min(\hat{V}_e,0)[N_{g,E}-C_o\varphi(r_e^+)\Delta N_{g,e}^+]\\ &+\max(\hat{U}_u,0)[N_{g,U}+C_o\varphi(r_u^-)\Delta N_{g,u}^-]+\min(\hat{U}_u,0)[N_{g,P}-C_o\varphi(r_u^+)\Delta N_{g,u}^+]\\ &-\max(\hat{U}_d,0)[N_{g,P}+C_o\varphi(r_d^-)\Delta N_{g,d}^-]-\min(\hat{U}_d,0)[N_{g,D}-C_o\varphi(r_d^+)\Delta N_{g,d}^+]\\ &+\max(\hat{W}_s,0)[N_{g,S}+C_o\varphi(r_s^-)\Delta N_{g,s}^-]+\min(\hat{W}_s,0)[N_{g,P}-C_o\varphi(r_s^+)\Delta N_{g,s}^+]\\ &-\max(\hat{W}_n,0)[N_{g,P}+C_o\varphi(r_n^-)\Delta N_{g,n}^-]-\min(\hat{W}_n,0)[N_{g,N}-C_o\varphi(r_n^+)\Delta N_{g,n}^+]+S_{N_g}\end{aligned} \tag{92}$$

where S_{N_g} is the total source, $C_0 = 0.5$ and all the terms are calculated at 'time' step n except when indicated by a superscript $n-1$. In (92) the gradients ΔN and the 'superbee' compressive flux limiter function of Roe (1985) are defined as:

$$\begin{aligned}\Delta N_{g,e}^+ =& N_{g,EE}-N_{g,E}, \quad \Delta N_{g,e}^- = N_{g,P}-N_{g,W},\\ \Delta N_{g,w}^+ =& N_{g,E}-N_{g,P}, \quad \Delta N_{g,w}^- = N_{g,W}-N_{g,WW}\end{aligned} \tag{93}$$

etc.

$$\varphi(r) = \max[0, \min(2r,1), \quad \min(r,2)] \tag{94}$$

where r is the ratio of consecutive gradients and is defined as:

$$\begin{aligned}r_e^- =& \frac{N_{g,E}-N_{g,P}}{N_{g,P}-N_{g,W}}, \quad r_e^+ = \frac{N_{g,P}-N_{g,W}}{N_{g,E}-N_{g,EE}},\\ r_w^- =& \frac{N_{g,P}-N_{g,W}}{N_{g,W}-N_{g,WW}}, \quad r_w^+ = \frac{N_{g,W}-N_{g,P}}{N_{g,P}-N_{g,E}} \quad \text{etc.}\end{aligned} \tag{95}$$

For the momentum equations $C_o = 0$ and the source term is partitioned into terms that depend on the solution at point P and those that are independent of the solution at P, incorporating

the former term into the diagonal of the matrices, resulting in a more diagonal dominant and stable system. Complete details of the computational method used to solve the gas equations have been given by Carrica et al. (1997).

The liquid momentum and mass conservation equations were solved with the CFDSHIP–IOWA code developed by Tahara et al. (1992) and Stern et al. (1996), in a modified form to account for the presence of gas bubbles, as shown in (88) and (89). Here we will only give an outline on the numerical method. For details the reader should see the references cited. The equations are reduced to algebraic form using a 12-point finite-analytic method. A pressure equation is obtained using the continuity equation in discrete form on as staggered-grid control volume. The overall solution method for the liquid equations is based on the PISO algorithm, in which the velocity and pressure fields are coupled using an iterative procedure assuming that the liquid volume fraction is known. In a first step, the pressure equation is solved using a tridiagonal algorithm and the method of lines to get an intermediate pressure. In the second step, the intermediate pressure is used to solve explicitly the momentum equation and the pressure updated.

3.4. Boundary conditions and solution domain

The FF-1052 is a Navy frigate which is $L = 126.7$ m long with a transom stern and a bulbous bow to accommodate a sonar dome. The nominal speed was 27 knots (13.5 m/s), which results in full-scale Reynolds and Froude numbers of $Re = 1.7 \times 10^9$ and $Fr = 0.39$. The computational conditions for the liquid were zero Froude number and $Re = 1 \times 10^6$. To calculate higher Reynolds numbers it would be necessary to refine the grid (Paterson et al., 1996). However, the Froude number in the gas equations must be kept as in the full-scale ship to obtain proper bubble behavior.

The calculation grid had $78 \times 21 \times 22$ (36,036) nodes in the ξ, η and ζ directions in H-grid topology. Cuts of the grid are shown in Fig. 2. The first row of nodes is located within $y^+ < 2$, in accordance to the Baldwin–Lomax turbulence model requirements.

The solution domain is shown in Fig. 2. A two-block approach was used to accommodate the regions from the inlet to the stern (block 1, $x/L = -0.4$ to $x/L = 1$) and in the wake (block 2, $x/L = 1$ to $x/L = 2$). At the interface between the two blocks, a parametrically-mapped bilinear-interpolation scheme was used to interpolate all the dependent variables in the overlapping planes in each block (Stern et al., 1996). The radial distance from the axis extends to a maximum $r/L = 1$. Only half of the domain was calculated, taking advantage of the symmetry of the problem.

The boundary conditions for the liquid and gas at the different boundaries in the physical domain are:

3.4.1. Inlet, $x/L = -0.4$

It was assumed that the inlet is far enough from the bow of the ship so that free stream conditions were used. The liquid velocities and pressure gradient are:

$$u_l = u_g = 1, \quad v_l = v_g = 0, \quad w_l = w_g = 0, \quad \frac{\partial p}{\partial x} = 0. \tag{96}$$

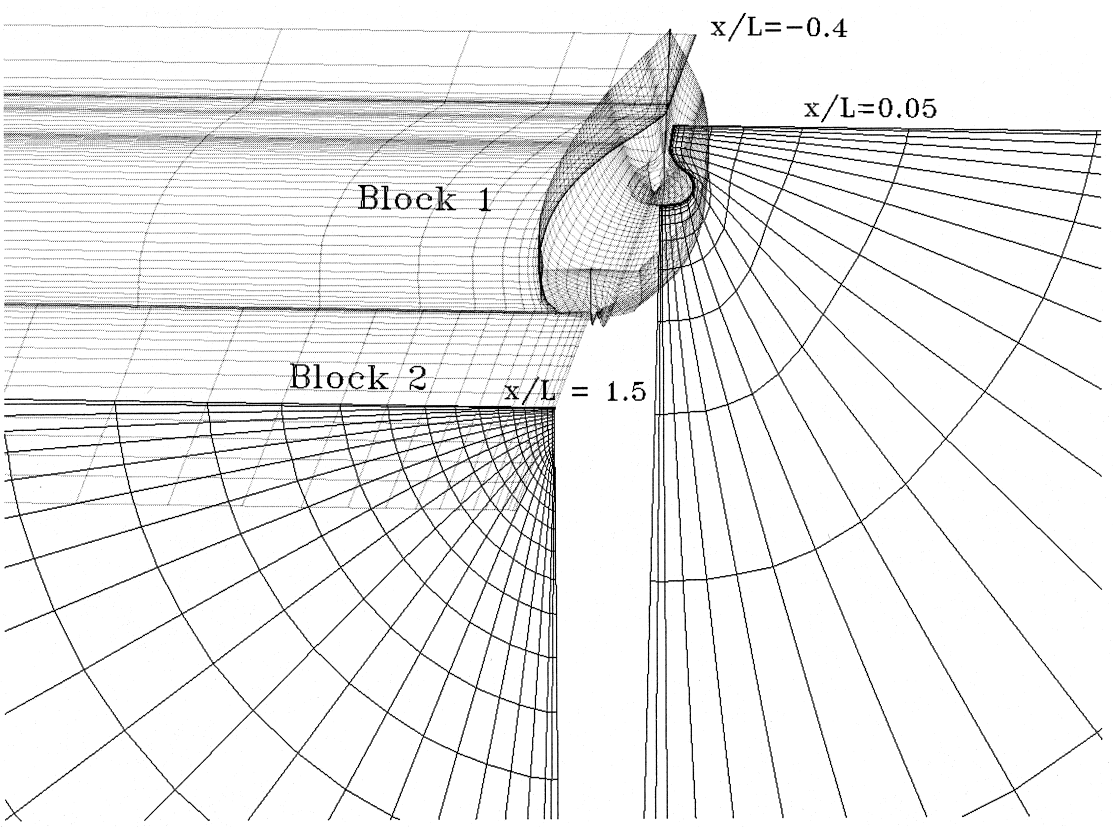

Fig. 2. Multi-block grid. The $z = 0$, $x/L = 0.05$ and $x/L = 1.5$ planes are shown along to the hull of the ship. All the grid is on the starboard side of the ship (right), but the planes in the left were flipped for clarity.

For the gas phase, it was assumed that no bubbles were present in the background ocean, so for each group the bubble number density was set to zero and the velocity was set equal to the liquid velocity. The only bubbles present will be those simulating a bow breaking wave.

3.4.2. Exit, $x/L = 2$

For the liquid, zero gradient conditions were used

$$\frac{\partial u_l}{\partial x} = \frac{\partial v_l}{\partial x} = \frac{\partial w_l}{\partial x} = \frac{\partial p}{\partial x} = 0 \tag{97}$$

and for the gas equations, free flux conditions were used. This means that the bubbles are free to leave the computational domain and the bubble concentration gradients, to calculate the turbulent dispersion force, are set to zero in the axial direction.

3.4.3. Hull and centerplane, $\eta = 0$ and $\zeta = 0$

Solid wall (hull) or symmetry conditions (centerplane), there was no gas or momentum flux. For the liquid equations, the conditions were:

$$u_l = 0, \quad v_l = 0, \quad w_l = 0 \quad \text{(hull)}, \tag{98}$$

$$\frac{\partial u_l}{\partial y} = \frac{\partial w_l}{\partial y} = \frac{\partial p}{\partial y} = v_l = 0 \quad \text{(centerplane)}. \tag{99}$$

3.4.4. Outer boundary, at $\eta = \eta_{max}$

Free flow for the gas. For the liquid equations

3.4.5. Free surface

The bubbles are free to leave the control volume and no bubbles are allowed to enter except at the entrance region that will be discussed later. For the liquid $Fr = 0$ conditions were used:

$$\frac{\partial u_l}{\partial z} = \frac{\partial v_l}{\partial z} = w_l = \frac{\partial p}{\partial z} = 0. \tag{101}$$

For the free flow conditions, the flux through the free flow surface was calculated using the velocity at the point P. For instance, if the free flow surface is given by $\zeta = \zeta_{\max}$, the balance equation for ϕ ($\phi = N_g, u_g, v_g, w_g$) in one control volume at $\zeta_{\max}$ reads:

$$C_P \phi_P = \sum_{k=u,d,e,w,s} C_k \phi_k + C_n \phi_P + S_{\phi,P}. \tag{102}$$

The condition of no gas or momentum flux was calculated by setting the flow through the appropriate control volume face equal to zero. For example, at the hull or centerplane ($\eta = 0$) the west face must have zero convection, so this was specified as:

$$C_P \phi_P = \sum_{k=u,d,e,s,n} C_k \phi_k + S_{\phi,P}. \tag{103}$$

3.5. Air entrainment

The air entrainment mechanisms for a surface ship is currently a subject of active research. This gas entrainment has two main sources. One source is bubbles generated by air entraining processes related to surface-hull interaction such as breaking and spilling waves at the bow and stern and boundary layer entrainment along the hull. The other source is the bubble production by the propellers that can cause growth of air bubbles in low pressure regions, mainly under cavitation conditions. Vapor cavitation bubbles can act as nucleation sites for diffusion-generated air bubbles. Unfortunately, the present knowledge in the subject is insufficient to properly simulate the gas entrainment processes under the given conditions.

Therefore, in this work we will assume that the gas is being entrained at the bow due to breaking waves situated between $x/L = 2.7 \times 10^{-3}$ and $x/L = 2.9 \times 10^{-2}$ and from 0.4 m to 1.7 m from the hull. The liquid and gas were assumed to be plunging in this area with vertical velocity −2.7 m/s, corresponding to a wave height of about 0.4 m, and the total void fraction was assumed to be 10%, in accordance with the typical void fractions obtained in plunging jet experiments (Bonetto and Lahey, 1993). The bubble size distribution was assumed to be that measured by Cartmill and Su (1993), who studied the bubble radius distribution for a breaking wave in salt water from 34 μm to 1200 μm. A total of 15 size groups were used with bubble radius at normal pressure between 10 μm and 1000 μm.

The system used by Cartmill and Su was not able to measure bubbles with radii smaller than 34 μm, and in that region their results were extrapolated. A similar approximation was used for bubbles larger than 1000 μm. The group limiting mass values (34) were the average of the two consecutive group masses and $m_{1-1/2} = 0$ and $m_{15+1/2} = \infty$. This distribution is shown in Table 1, and we will refer to it as the reference distribution.

Numerically, this set of assumptions results in a Dirichlet boundary condition for both group void fraction and velocity, to be applied in the air entrainment region.

3.6. Solution procedure

The equations were solved iteratively using a pseudo-transient marching process in the x-direction and the method of lines at each perpendicular plane. The convergence was evaluated measuring the L_2 norm of the different independent variables. A variable was considered converged when the decrease in the L_2 norm was more than three orders of magnitude.

To achieve convergence, it was necessary to overrelax the gas momentum equations with increasing relaxation constants of about 1×10^{-4} in the last iterations. Higher relaxation

Table 1
Size distribution at the air entrainment boundary conditions

Group	m_g (kg)	$r_{g,0}$ (μm)	N_g (1/m^3)	ε_g (%)
1	4.82×10^{-15}	10.0	2.61×10^{10}	0.0109
2	4.46×10^{-14}	21.0	6.31×10^{9}	0.0245
3	2.03×10^{-13}	35.0	2.97×10^{9}	0.0524
4	7.20×10^{-13}	53.0	1.69×10^{9}	0.106
5	2.24×10^{-12}	77.5	1.04×10^{9}	0.204
6	6.34×10^{-12}	109.6	6.01×10^{8}	0.332
7	1.66×10^{-11}	151.0	2.95×10^{8}	0.426
8	4.05×10^{-11}	203.5	1.51×10^{8}	0.531
9	9.26×10^{-11}	268.0	8.08×10^{7}	0.651
10	2.00×10^{-10}	346.5	4.50×10^{7}	0.784
11	4.11×10^{-10}	440.5	2.60×10^{7}	0.931
12	8.07×10^{-10}	551.5	1.56×10^{7}	1.09
13	1.52×10^{-9}	680.5	9.56×10^{6}	1.26
14	2.75×10^{-9}	829.5	6.06×10^{6}	1.45
15	4.81×10^{-9}	1000.0	5.13×10^{6}	2.14

constants led to strong oscillations in the solution near the wall. These oscillations disappeared for large Schmidt numbers Sc_b, showing the convenience of running first a high Schmidt number case ($Sc_b = 5$) and then using this solution as the starting point for the case with $Sc_b = 1$ and more relaxation.

The program needed 10 megawords of memory to run on a Cray C90 machine. Each case took about 200 CPU h to converge. Approximately 30% of this CPU time was consumed in the intergroup transfer subroutines.

4. Results and discussion

4.1. Size distribution

The bubble size distribution is of major importance in the two-phase flow around a ship for several reasons. On one hand, the acoustical response on the wake of the ship is strongly dependent on bubble radius distribution. On the other hand, the two-phase flow and size distribution in the wake depends on the interactions between the bubbles and the ship and with each other, as well as with the size distribution at the regions of air entrainment.

The simplest case that can be studied of a polydisperse two-phase flow is that with no intergroup transfer source, in other words with no dissolution, breakup or coalescence. In this case, the bubbles cannot change their mass, however the bubble size distribution still may change because of accumulation or depletion of certain bubble sizes in certain regions. Also, all the groups contribute to the coupling of the liquid through the total void fraction.

The study of the bubble size distribution was made for five different conditions: with no intergroup transfer source, with a coalescence source, with a breakup source, with a dissolution source and with all the sources. In this way the individual effect of each of the intergroup transfer terms can be evaluated, and the sensitivity to each exchange process assessed.

Figures 3–5 show the distribution function, group number density and group void fraction normalized to 1.0 at the hull of the ship at $x/L = 0.95$, 25 cm below the surface, close to the point where the maximum void fraction occurs in the case with no intergroup sources. The five different conditions explained above are shown. The total number density is 1.65×10^{10} l/m^3 for the case with no intergroup exchange and 2.22×10^{10} l/m^3 for the complete model, this last number being higher mainly due to the effect of tipstreaming, which generates a large amount of small bubbles. The total absolute void fraction reaches 0.261 for the complete model and 0.263 with no intergroup sources, but in the complete model, the void fraction is more evenly distributed compared to the model with no sources, in which case, the big bubbles are responsible for most of the gas present. When only coalescence is included, the concentration of small bubbles falls considerably due to the high collision rate observed in this region of very high void fraction due to buoyancy-driven gas accumulation. Also, a high bubble breakup rate occurs all along the hull due to the high shear rates present in the boundary layer. This is evident from the depletion of large bubbles that is predicted in the breakup case compared to the case with no sources, and from the peak in the distribution at small bubble sizes resulting from tipstreaming. Also, dissolution plays a very important role in this region because of the low velocities near the hull and the consequent large transit times that allow large intergroup

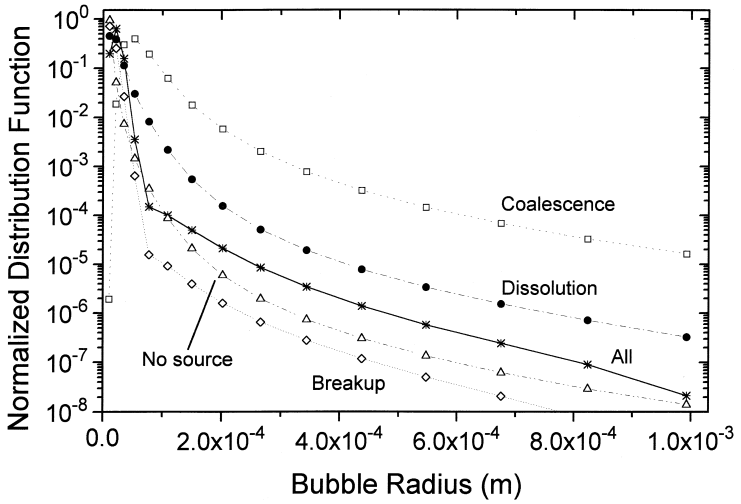

Fig. 3. Effect of the different intergroup transfer mechanisms on the normalized distribution function at $x/L = 0.95$ at the hull of the ship, 25 cm below the water surface.

and mass transfers. As can be seen in (27) and (28), the radius change rate due to dissolution is higher for small bubbles. The complete multigroup case shows that, at this position, breakup plays the most important role in the determination of the shape of the size distribution.

Figures 6–8 show the effect of the different intergroup sources on the distribution function, group number density and group void fraction normalized to 1 at the near wake region of the ship ($x/L = 1.5$, $y/L = 0.04$). The point is coincident with the main stream of bubbles in the wake and is located 2.15 m below the surface of the ocean, where the hydrostatic pressure effects become important. At this depth, the big bubbles have naturally disappeared by

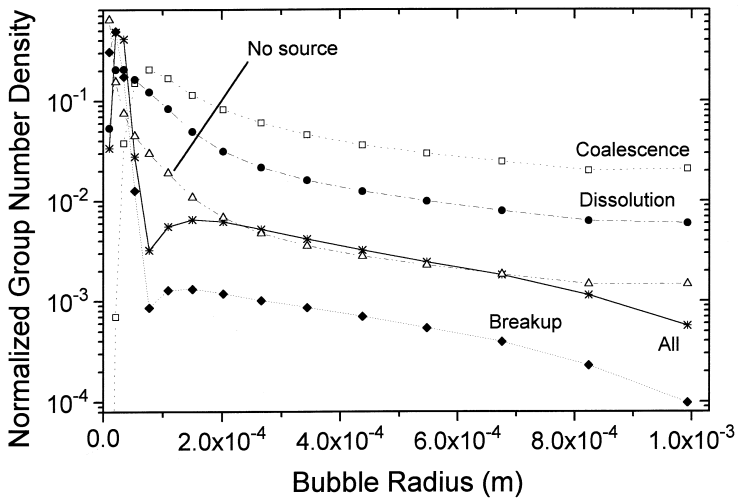

Fig. 4. Effect of the different intergroup transfer mechanisms on the normalized group number density at $x/L = 0.95$ at the hull of the ship, 25 cm below the water surface.

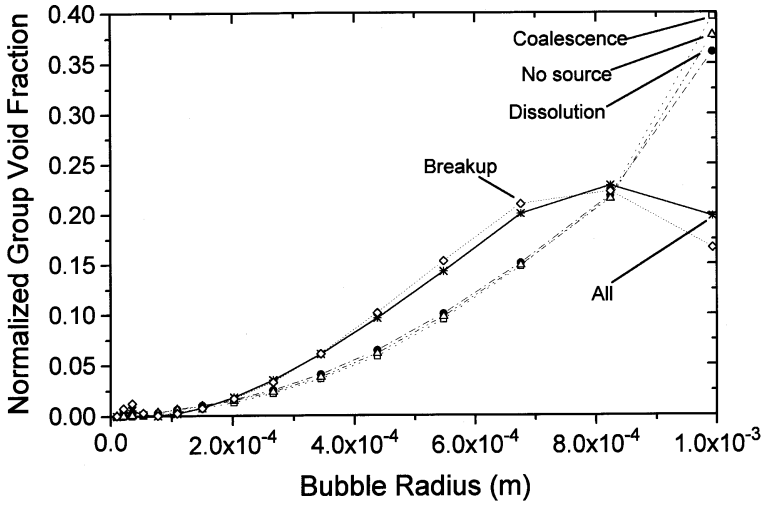

Fig. 5. Effect of the different intergroup transfer mechanisms on the normalized group void fraction at $x/L = 0.95$ at the hull of the ship, 25 cm below the water surface.

buoyancy and their contribution to the void fraction has been drastically reduced, thereby resulting in a peak in the group void fraction for medium-sized bubbles. In the case of only breakup, an additional peak appears for the bubbles arising from tipstreaming, but this peak is not present in the full model. At this depth in the wake, breakup and tipstreaming have less effect than in the near hull region. This is probably due to the fact that the bubbles accumulate at the hull, under the ship, and therefore, are subject to strong breakup. They will detach at the stern at about 1 m depth. From there only a few of them can reach deeper points due to turbulent dispersion. At this point, dissolution appears to be the most important intergroup

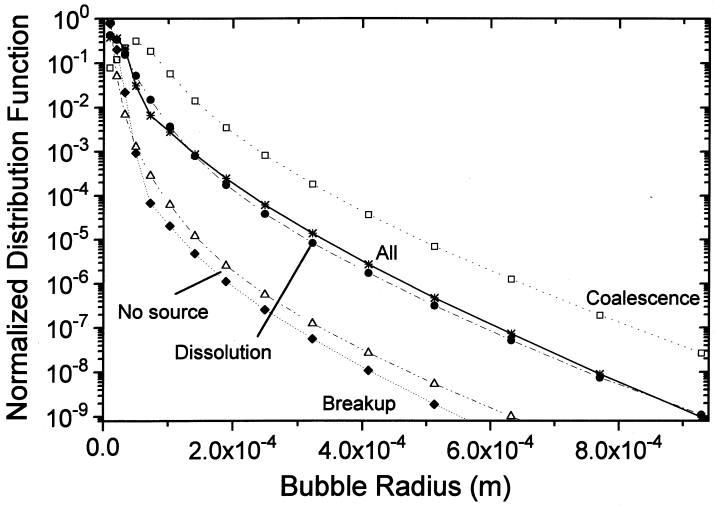

Fig. 6. Effect of the different intergroup transfer mechanisms on the normalized distribution function at the wake, at $x/L = 1.5$, $y/L = 0.04$, $z = -2.15$ m.

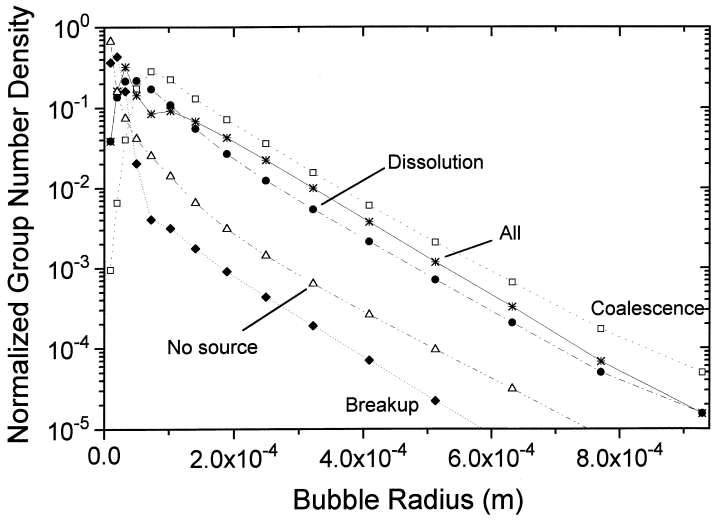

Fig. 7. Effect of the different intergroup transfer mechanisms on the normalized group number density at the wake, at $x/L = 1.5$, $y/L = 0.04$, $z = -2.15$ m.

transfer mechanism for determining the size distribution. This is evidenced by the much smaller dimensionless total number density in the complete multigroup model (3.66×10^8 l/m^3) compared to the case with no intergroup exchange sources (5.95×10^9 l/m^3). This loss of small bubbles causes the total void fraction to fall from 0.004 in the case with no sources to 0.0029 in the complete model.

Shown in Figs. 9–11 are the distribution function, group number density and group void fraction at different locations in the calculation domain for the complete intergroup source. The locations are at the hull at the same point as in Fig. 3, at the wake at $x/L = 1.5$,

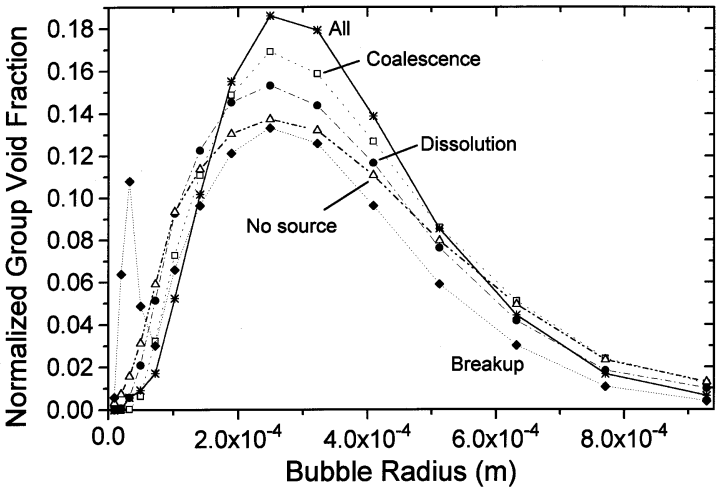

Fig. 8. Effect of the different intergroup transfer mechanisms on the normalized group void fraction at the wake, at $x/L = 1.5$, $y/L = 0.04$, $z = -2.15$ m.

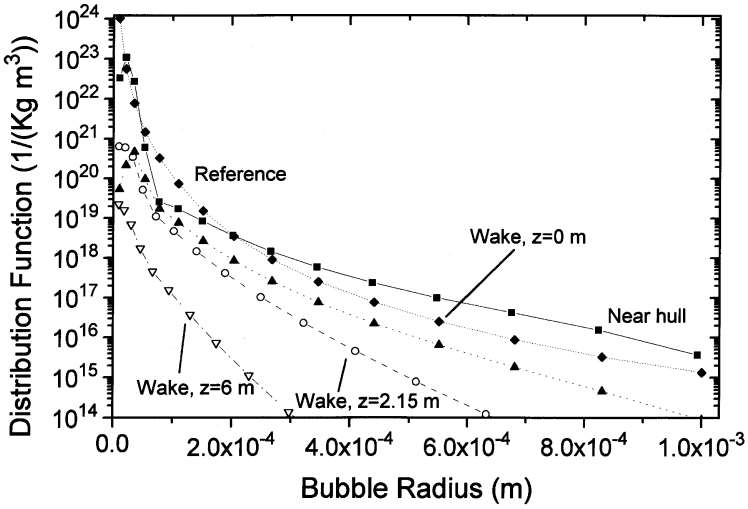

Fig. 9. Distribution function at different locations: at the hull (same as Fig. 5); at the wake, at $x/L = 1.5$, $y/L = 0.04$, $z = 0$ m, -2.15 m, -6 m and at the air entrance.

$y/L = 0.04$ and depths 0 m, 2.15 m and 6 m. The reference distribution is also shown. The total number density and void fraction are (2.22×10^{10} l/m^3, 0.261), (5.06×10^{8} l/m^3, 0.0163), (3.66×10^{8} l/m^3, 0.0029) and (9.54×10^{6} l/m^3, 0.00003) at the hull, and at the wake at 0, 2.15 and 6 m, respectively. At the air entrainment point, these values are (3.93×10^{10} l/m^3, 0.1). It can be seen that gas accumulation occurs at the hull, mainly due to large bubbles. Due to tipstreaming, a significant number of small bubbles are generated in this region, but as their volume is small, they have a very small void fraction. In the wake, the effects observed at the hull are less important at deeper positions. The density of big bubbles decreases very fast at greater depths, where only small bubbles remain.

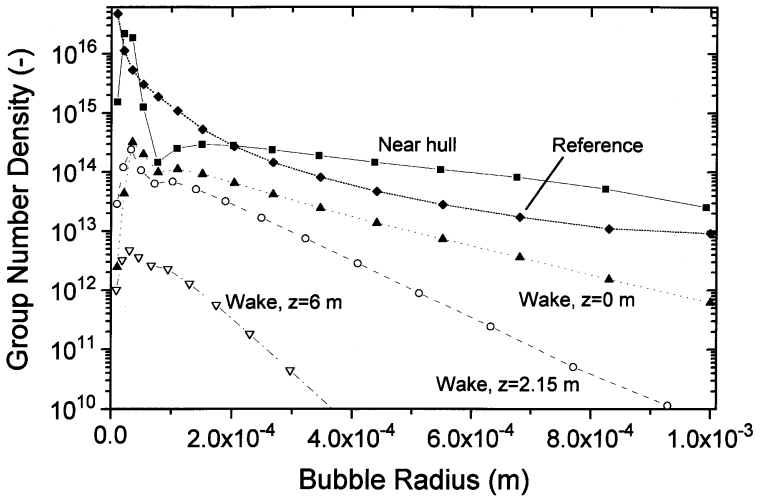

Fig. 10. Group number density at different locations, at the same points as in Fig. 9.

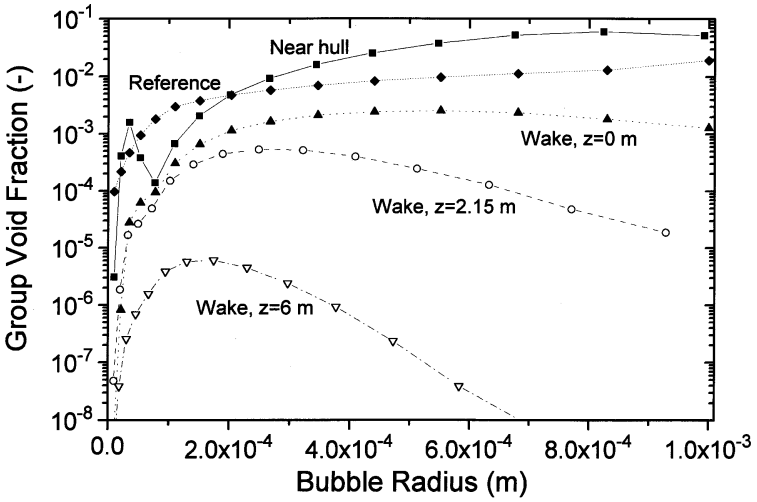

Fig. 11. Group void fraction at different locations, at the same points as in Fig. 9.

To clarify the size distribution at different locations, the normalized group void fraction at these locations is shown in Fig. 12. It can be seen that the peak in the void fraction distribution moves to smaller sizes as we go deeper in the wake, while at the hull, and for the reference distribution, the big bubbles dominate the void fraction distribution.

4.2. Integral quantities

The total bubble number density, interfacial area density and void fraction (2), (3) and (5) were calculated in the solution domain for the case without intergroup sources and for the complete model with breakup, coalescence and dissolution. In addition, the bubble average

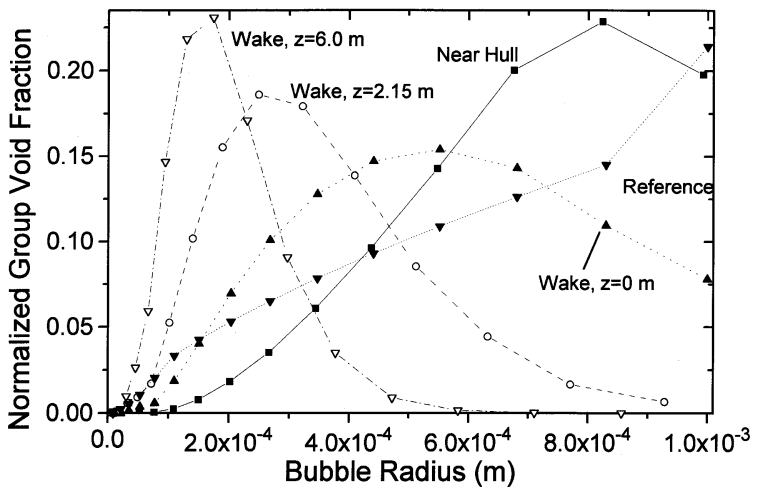

Fig. 12. Normalized group void fraction at different locations, at the same points as in Fig. 9.

radius, weighted with the bubble number density, and the gas superficial velocity were calculated and are defined as:

$$\bar{R}_{\mathrm{b}} = \frac{\sum_{g=1}^{NG} N_g R_g}{\sum_{g=1}^{NG} N_g}, \tag{104}$$

$$j_i = \sum_{g=1}^{NG} u_{g,i} \varepsilon_g. \tag{105}$$

Fig. 1 shows surface total void fraction contours and the FF 1052 hull. A distinct wake is formed that loses strength as the big bubbles are lost through the surface.

The dimensionless gas superficial velocity is shown in Fig. 13 for the complete multigroup model. The transversal cuts are at $x/L = 0.25$, 0.6, 0.95 and 1.5. In the left side, contour lines of the axial component (j_1) are shown, and in the right side, the vector plots of the transversal components (j_2, j_3) are depicted. It can be seen that, as the bubbles move towards the stern, there is some gas accumulation at the hull. The superficial velocity is always very small at the hull, however it is generally not zero because the gas velocity does not have to satisfy the zero slip condition. At $x/L = 0.25$ there is strong effect of the air entrainment boundary condition, and many bubbles are still being forced downwards by the liquid.

Fig. 14 shows the total void fraction at $x/L = 0.25$, 0.6, 0.95 and 1.5 for the cases of no intergroup source (left) and full model (right). Close to the hull, both profiles look qualitatively similar, though the constant void fraction lines are a little farther from the hull, showing more accumulation near the hull in the case with no intergroup exchange. In the wake, some important differences arise: for large depths, the case with sources shows less void fraction, mainly due to the effect of dissolution that reduces the amount of gas transported by the small bubbles that are mainly present in that location. On the other hand, close to the surface, the smaller number of big bubbles in the complete model reduces the loss of gas through the surface, resulting in a higher void fraction in this region.

Fig. 15 depicts the total bubble number density at the same crossplanes as Fig. 14, under the same conditions. In the case with no intergroup exchange, the total number density shows a peak near the hull at $x/L = 0.25$. This peak comes closer to the wall downstream as the bubbles accumulate, but at the wake, the big bubbles disappear through the surface. The smaller bubbles remain, resulting in a peak below the free surface. The case with dissolution, breakup and coalescence shows a different behavior. The small bubbles very soon dissolve or coalesce in the near wall region, and thus, the total number density is governed by medium size bubbles that attach to the hull. This causes the total number density to peak at the hull all along the ship, and at the free surface in the wake. The total number density is also considerably smaller than for the case with no intergroup exchange.

The total interfacial area density is shown in Fig. 16. The behavior is similar to that observed in the void fraction, with interfacial area accumulation at the hull, that becomes more

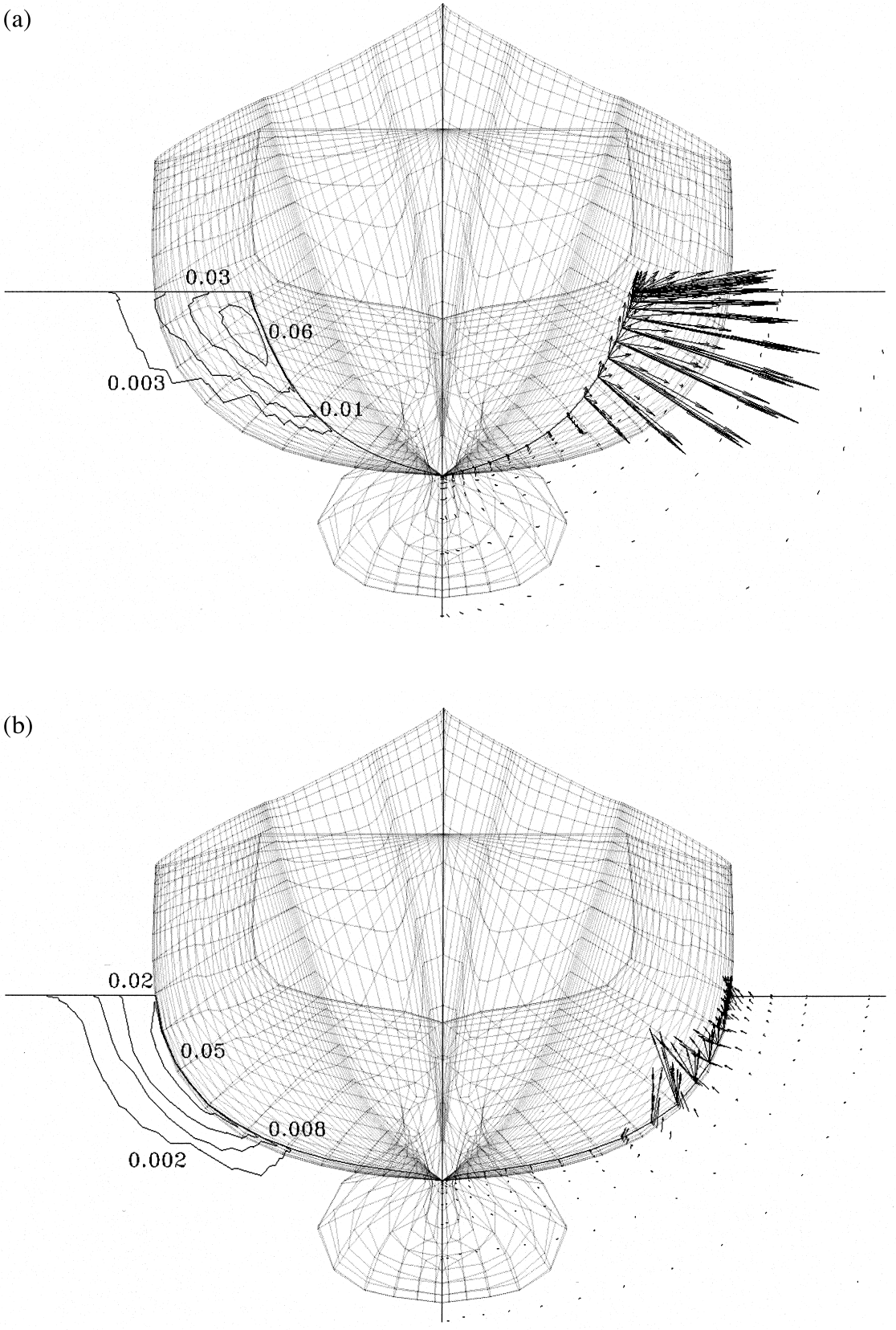
(a)
0.03
0.06
0.003
0.01
(b)
0.02
0.05
0.008
0.002

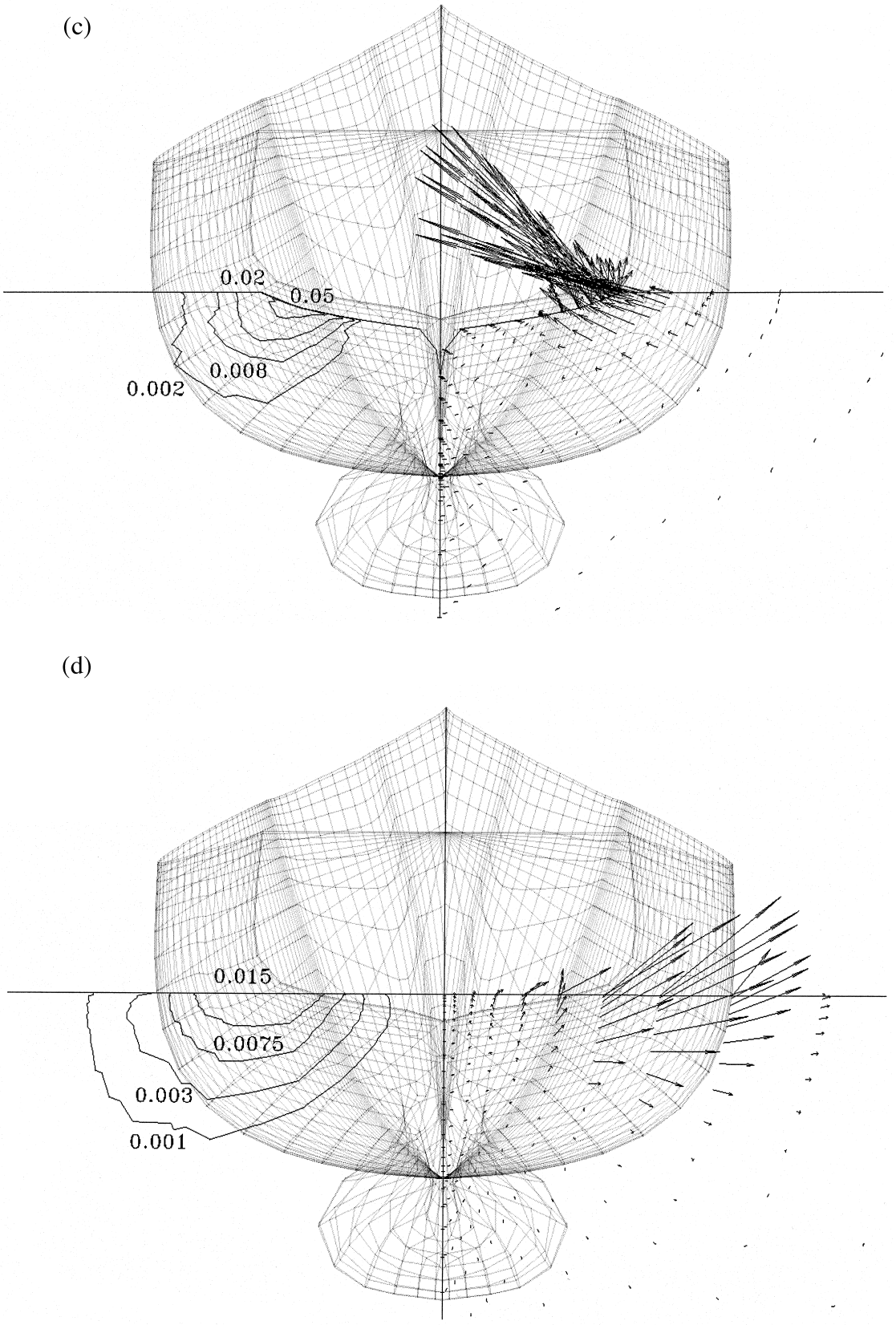

Fig. 13. Dimensionless gas superficial velocity at $x/L = 0.25$ (upper left), $x/L = 0.6$ (upper right), $x/L = 0.95$ (lower

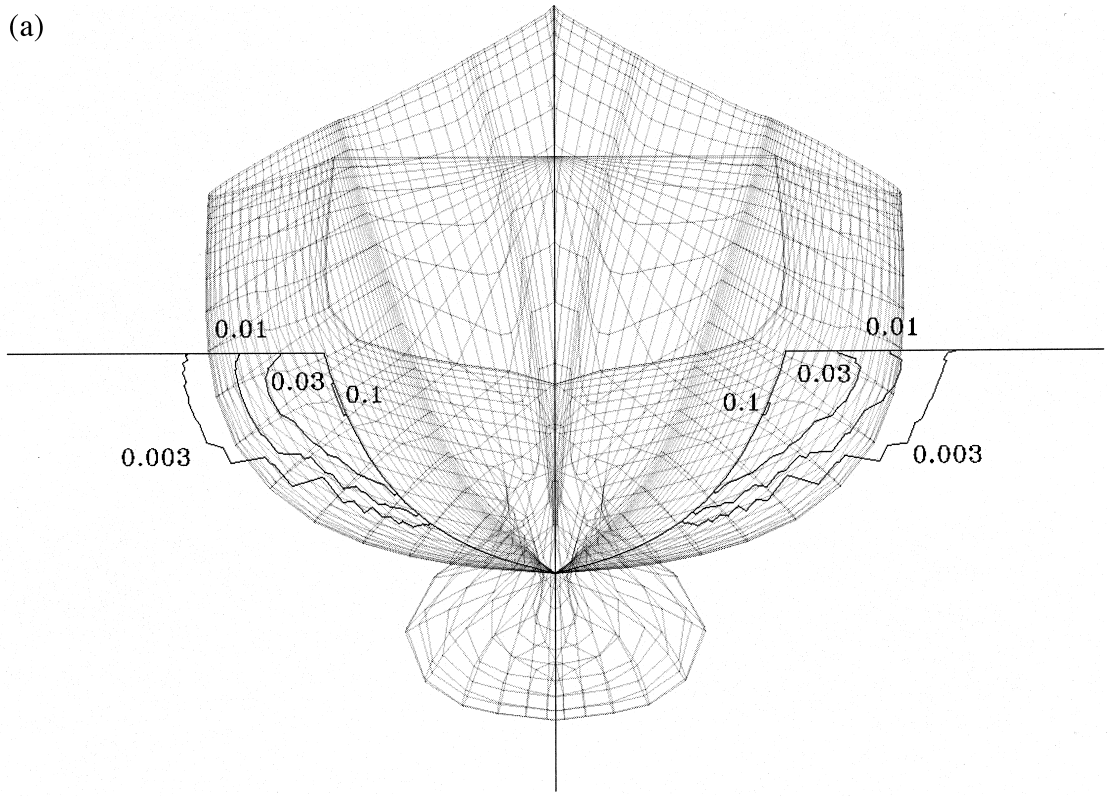
(a)
0.01
0.03
0.1
0.003
0.01
0.03
0.1
0.003

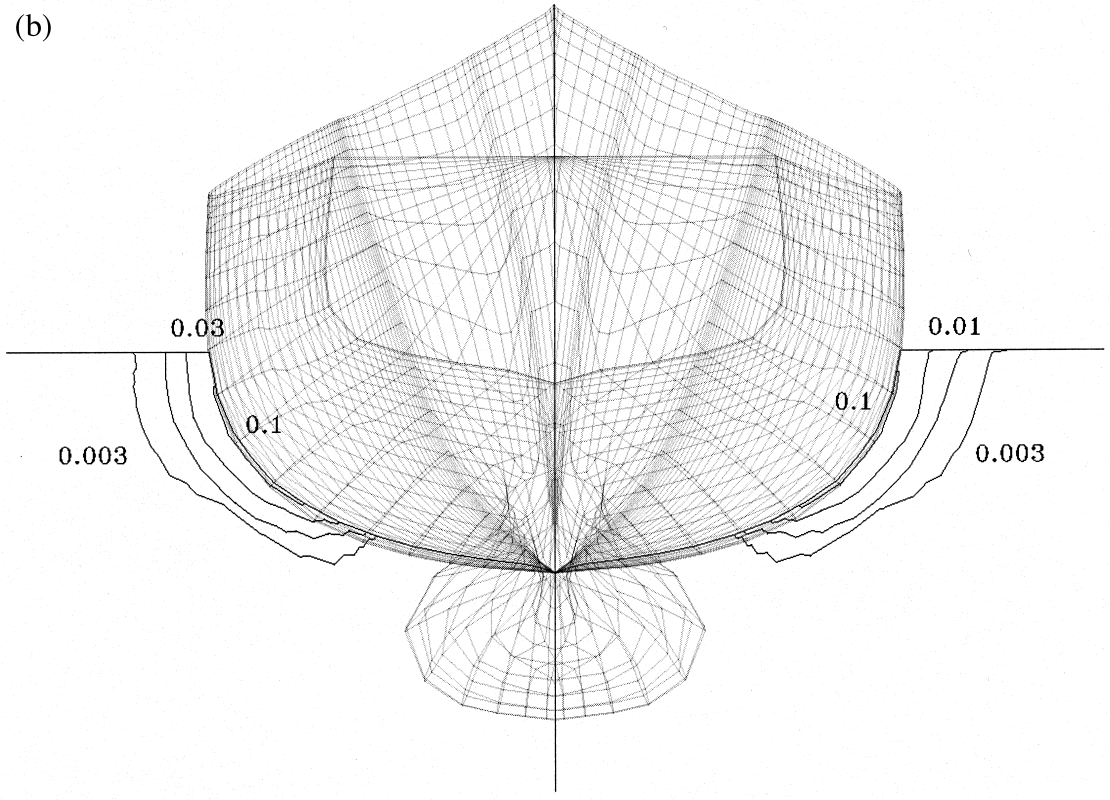
(b)
0.03
0.1
0.003
0.01
0.1
0.003

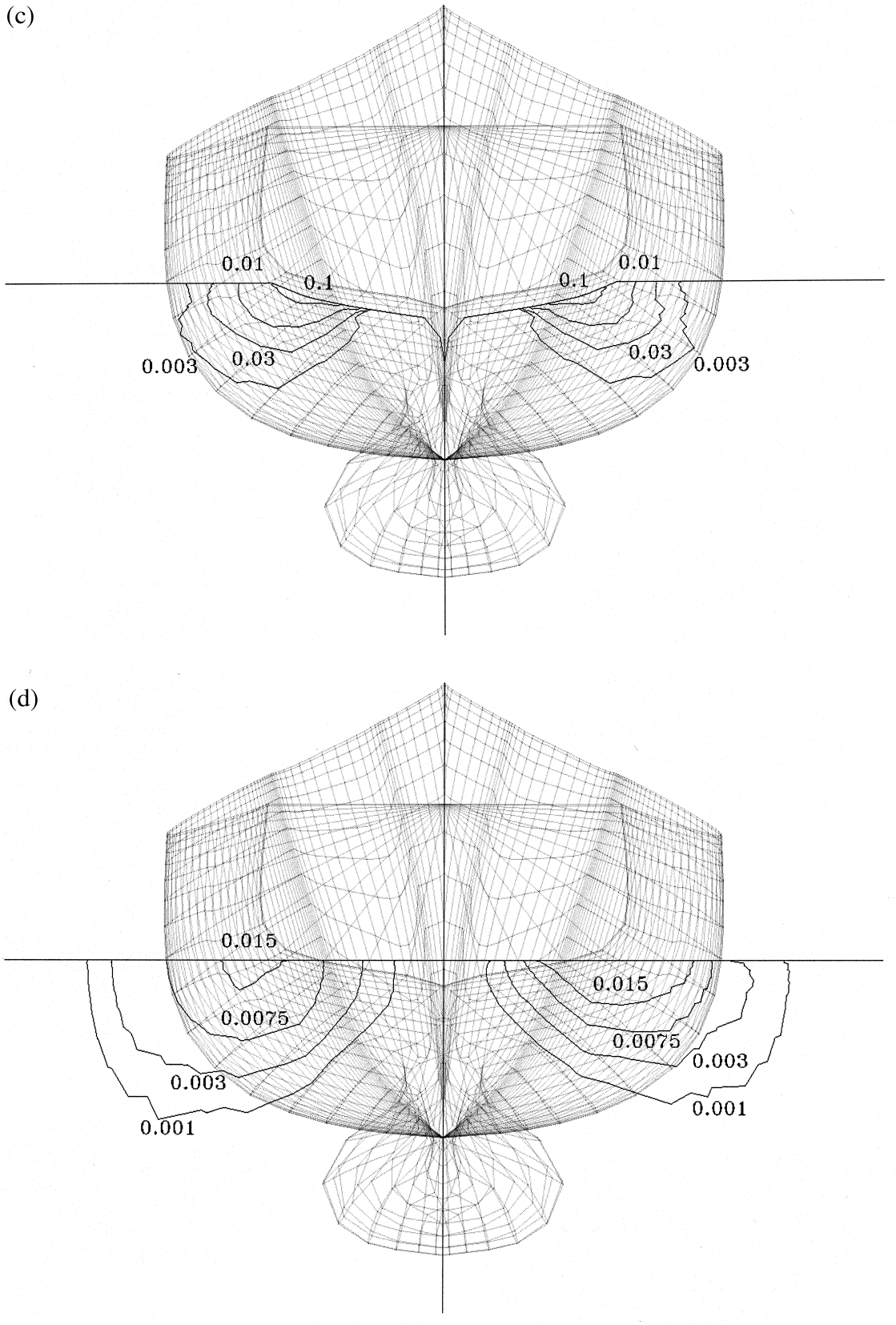

Fig. 14. Void fraction at $x/L = 0.25$ (upper left), $x/L = 0.6$ (upper right), $x/L = 0.95$ (lower left) and $x/L = 1.5$ (lower right). In each cut, the complete model case (right) and the case with no intergroup sources (left) are shown.

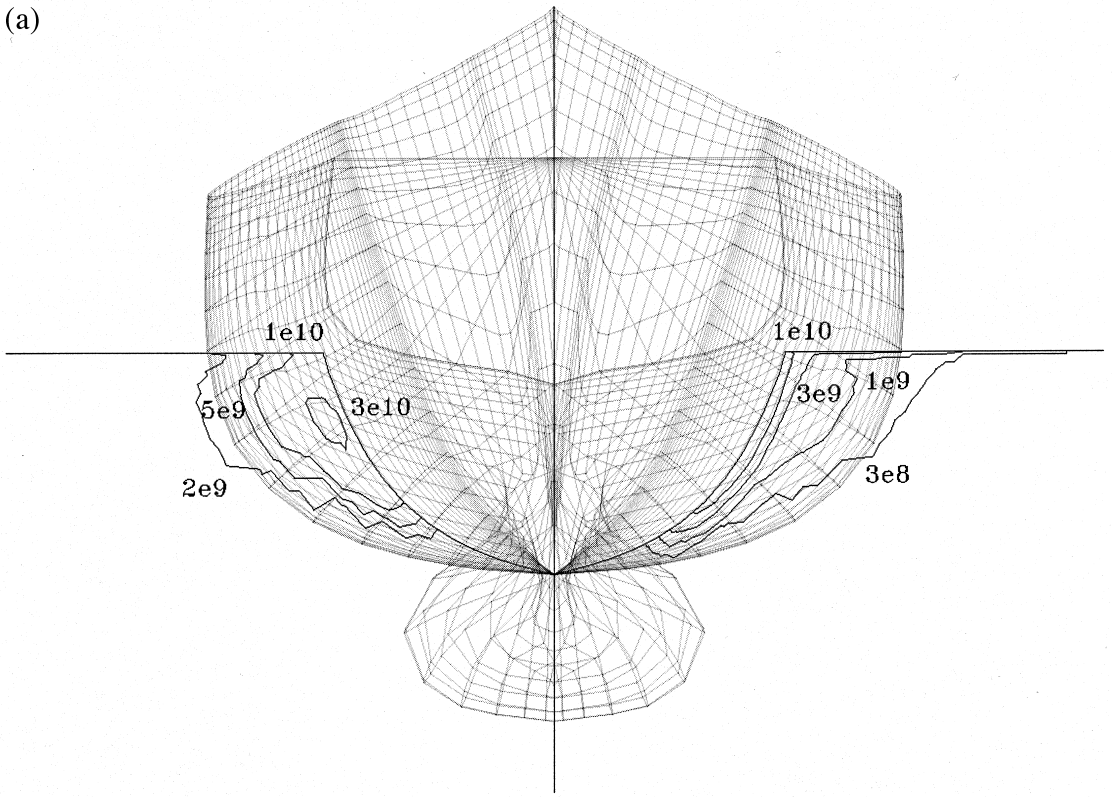
(a)
1e10
1e10
5e9
3e10
3e9
1e9
2e9
3e8

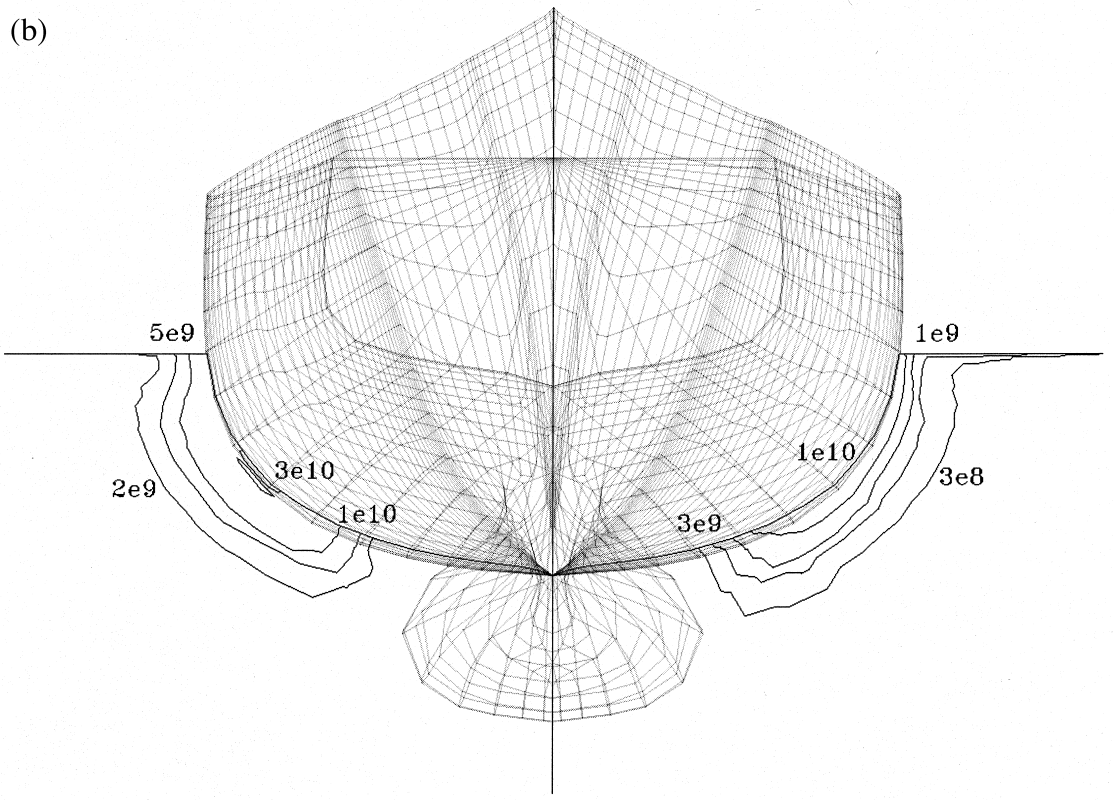
(b)
5e9
1e9
3e10
1e10
2e9
1e10
3e9
3e8

(c)

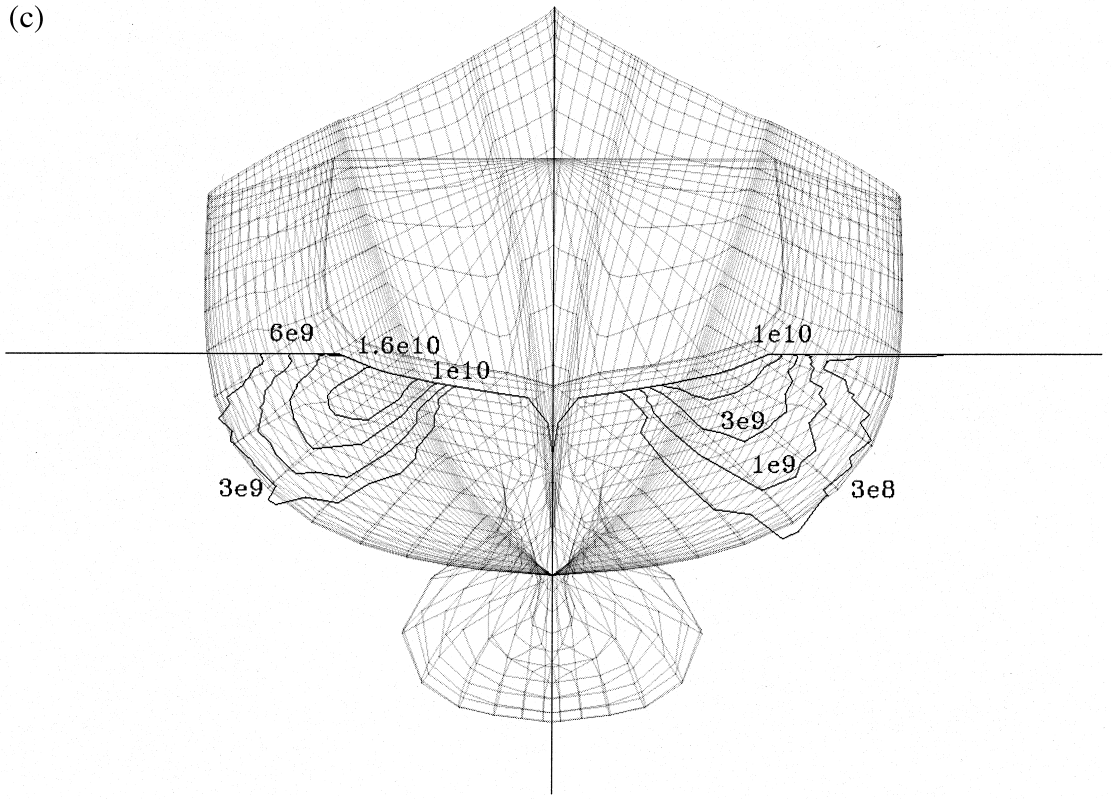
6e9
1.6e10
1e10
1e10
3e9
1e9
3e9
3e8

(d)

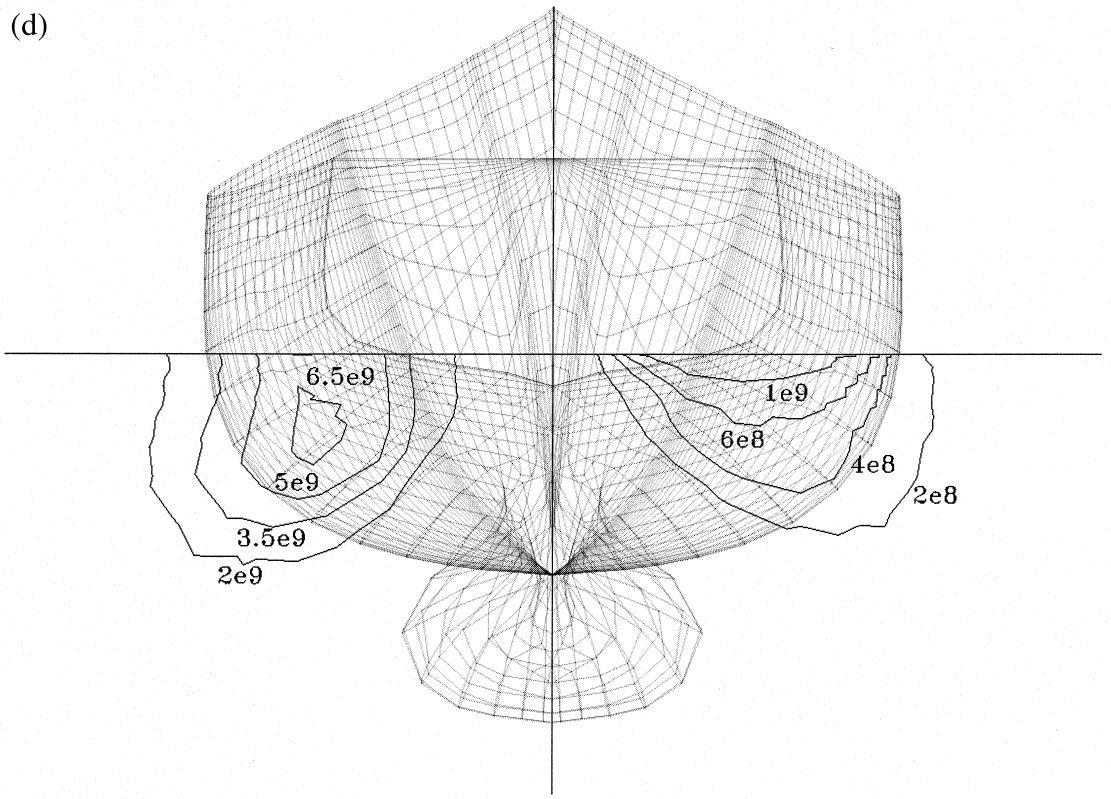
6.5e9
1e9
6e8
4e8
2e8
5e9
3.5e9
2e9

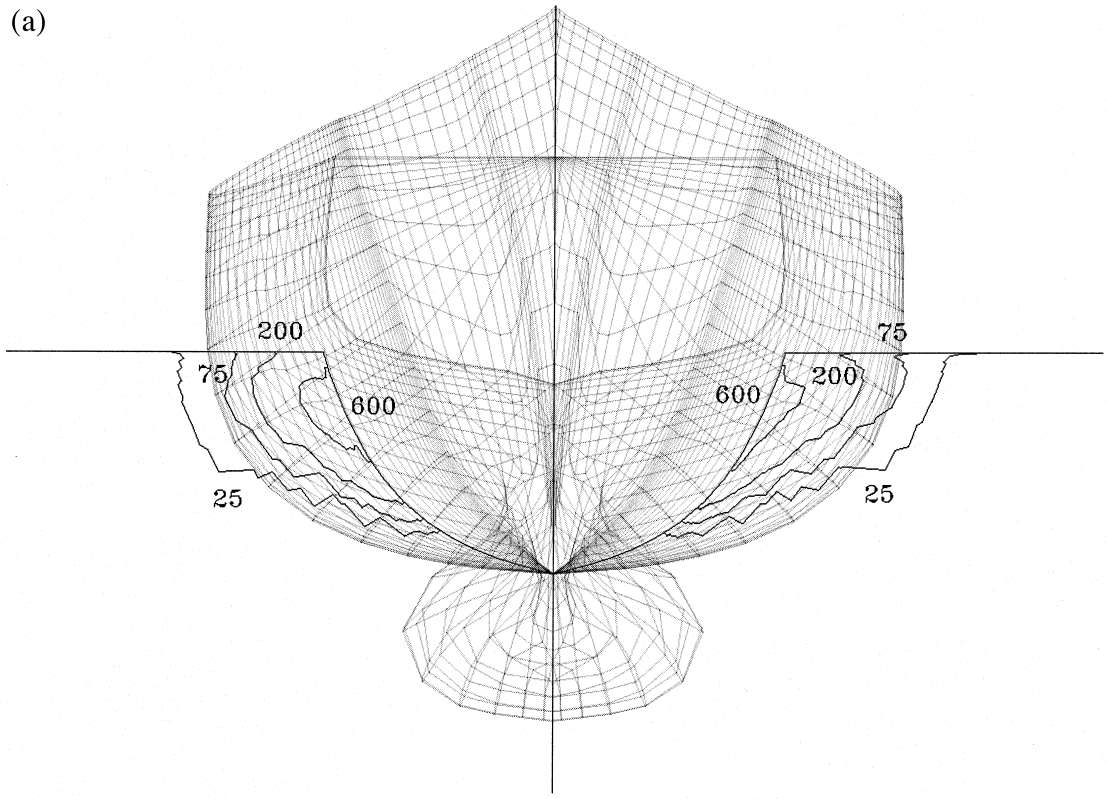
(a)
200
75
75
600
600
200
75
25
25

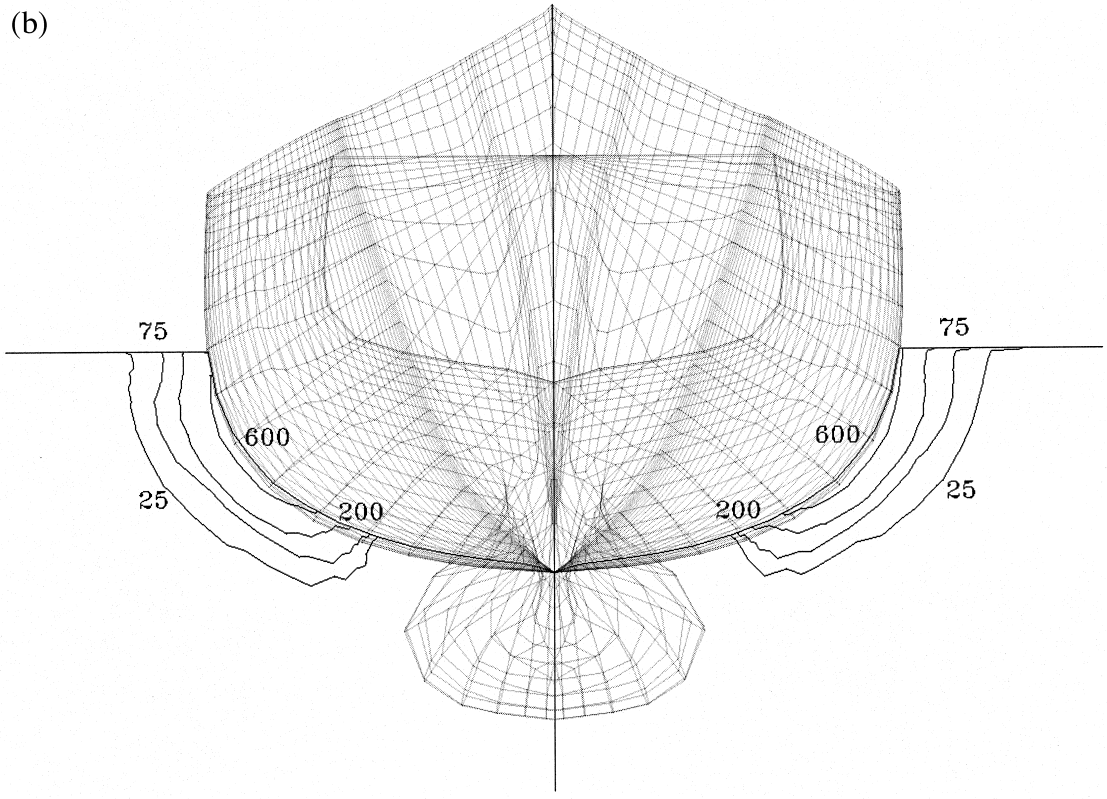
(b)
75
75
600
600
25
25
200
200

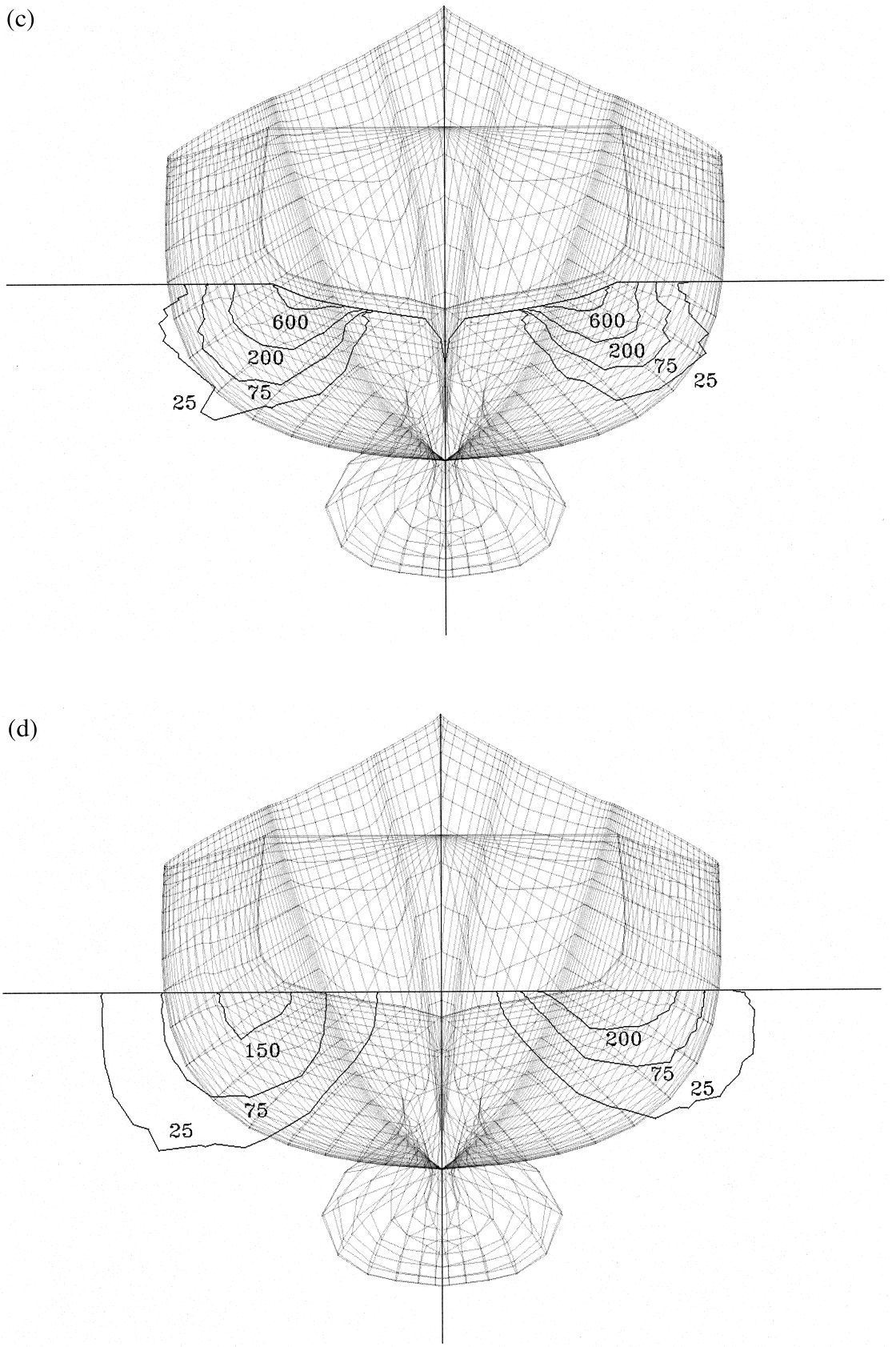
(c)
600
200
75
25
600
200
75
25
(d)
150
75
25
200
75
25

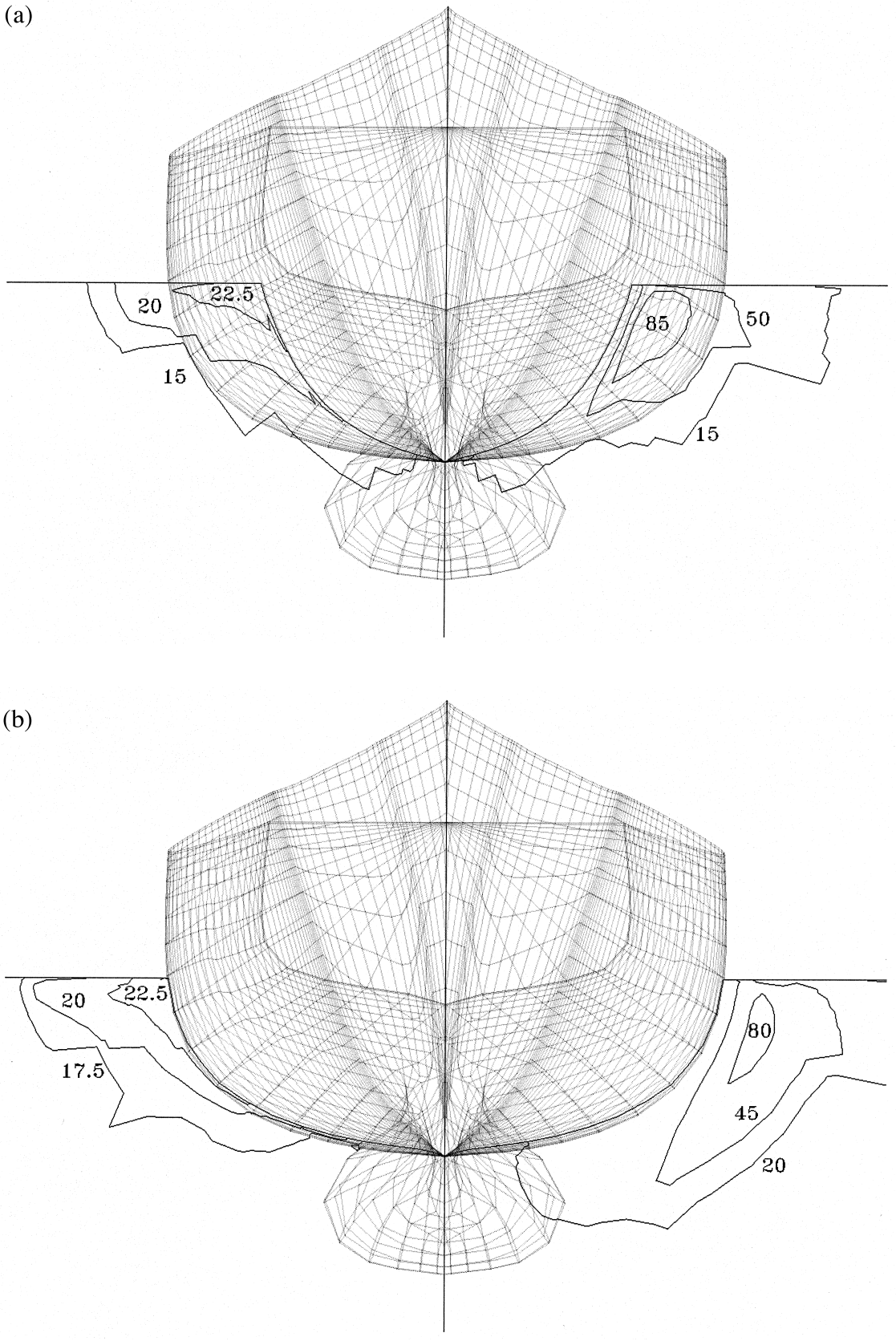
(a)
20
22.5
15
85
50
15
(b)
20
22.5
17.5
80
45
20

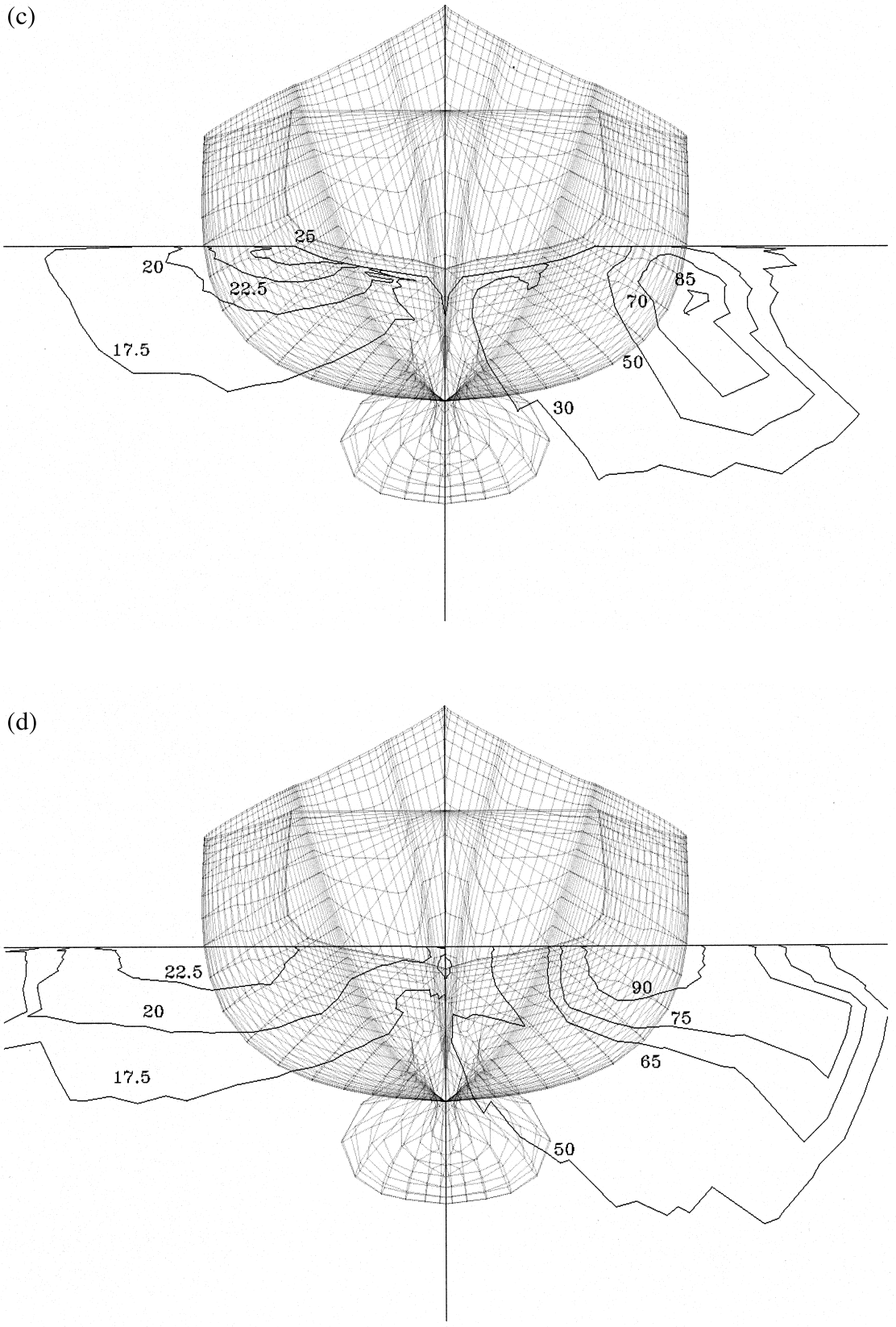

Fig. 17. Average radius (μm) at $x/L = 0.25$ (upper left), $x/L = 0.6$ (upper right), $x/L = 0.95$ (lower left) and

evident for the full model. In the wake, higher interfacial area is present near the surface in the full model, while deeper, the interfacial area is higher for the model with no sources.

The effect of the intergroup transfer sources on the average radius is very large. As shown in Fig. 17, the average radius is considerably larger for the case with intergroup exchanges than without them. The case without intergroup exchanges has maximum average radius at the hull or at the free surface because of the accumulation of large bubbles or the effect of the hydrostatic pressure. When coalescence and dissolution are present, the number of small bubbles decreases considerably and therefore the maximum radius is larger. Near the hull, the tipstreaming fixes the average radius on the order of 20–30 μm, and in the wake the average radius size is about three times the size obtained without sources. This result is very important because the bubble size will determine the acoustical response of the wake, and shows the importance of a proper modeling of the different mechanisms of intergroup transfer.

The superficial velocity through the free surface is shown in Fig. 18 for the cases with the full model (right) and without intergroup exchanges (left). As can be seen in the figure, most of the gas leaves the surface in the first ship length. If the gas entrance region is put closer to the hull, this effect would be more noticeable because more bubbles would be convected below the hull, coming back to the surface at the stern. This air liberation at the stern can be easily observed in this type of ship, though it is not clear at present if the primary source of those bubbles is breaking and spilling waves or aeration due to the propeller, or both. This result shows that it is very likely that breaking bow waves are responsible for at least part of the air leaving the free surface at the wake near the stern. In the case without intergroup exchange, the air liberation occurs closer to the hull than in the full model simulation.

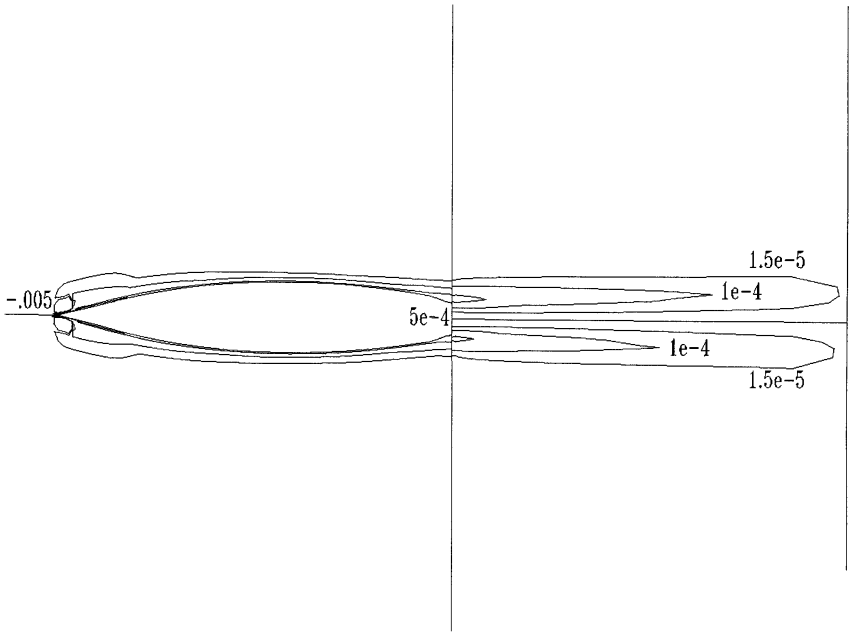

Fig. 18. Dimensionless vertical superficial velocity at the free surface. The left side shows the case without intergroup sources and the right side the complete model.

5. Uncertainty analysis

A grid sensitivity analysis has been performed, in an attempt to assess the numerical uncertainties of the calculations. Additionally, some sensitivity analysis to the model constants has been performed and reported elsewhere (Paterson et al., 1996; Carrica et al., 1997). Modeling uncertainties must be evaluated compared to experimental data and will be assessed in future works.

A careful analysis of the uncertainties for free-surface flow at $Re = 2.01 \times 10^7$ around an FF-1052 is discussed by Stern et al. (1996). They found that the thrust, friction and total resistance coefficients change about 2% between grids for grid sizes between 400,000 to 906,000 nodes. They estimate the total uncertainty in the propelled case, based on integral quantities, is on the order of 4%, though they recognize that their estimation may be optimistic. It must be noticed that at that high Reynolds number, the proper discretization of the boundary layer is critical to predict friction coefficients, thus forcing the use of very fine grids.

The assessment of the uncertainties in two-phase flow is much more complex, and a complete analysis has not been performed yet. The tremendous computational cost involved in such analysis has limited the number of test runs done to the present.

A grid convergence analysis for the variable size, monodisperse two-phase flow around a FF-1052 under free-surface conditions at a moderate Reynolds number ($Re = 2 \times 10^6$) has been done by the authors (Carrica et al., 1997). The study was done in 4 grids, with 36,036, 50,820, 75,020 and 176,000 nodes. The main conclusions drawn from that analysis are: the maximum void fraction close to the hull changes about 2.5% between the finer grids, and about 20% between the two coarser grids. However, outside the boundary layer, the change in the void distribution was less than 2% for all grids. It was also found that the better resolution of the boundary layer with finer grids has a limited effect on the overall bubble size and spatial distribution in the near wake. Other parameters depending on the flow near the hull, such as free surface shape, cannot be properly predicted with the coarsest grid.

The zero Fr number case (flat surface) can be simulated with coarser grids. Previous experience with several grids ranging from 7000 to 75,020 nodes have shown that at $Re = 1 \times 10^6$ the single-phase flow field can be simulated reasonably with small size grids. Based on this experience, we chose the coarsest grid (36,036 nodes) that shows reasonable results. The complete multigroup case was also tested in a finer grid ($110 \times 31 \times 22 = 75{,}020$ nodes). Between these two grids, the change in the pressure and friction coefficients was about 3%.

As in the monodisperse case, the main features of the two-phase flow changed only slightly. The maximum void fraction at the wall showed an increment of 1.5% for the fine grid with respect to the coarse grid, while the number density increased 4%. Outside the boundary layer and at the ship's wake, the changes were much smaller, lower than 2% for all the variables at each location.

The better resolution of the boundary layer for the fine grid compared to the coarse grid caused an increment of the breakup rate in the near-wall region, then slightly shifted the size distribution towards smaller bubbles, showing increases of up to 5% in the number density in the smallest groups. This increment of the group number density for small bubbles causes, in turn, an increment of the total number density of a maximum of 4%. However, this change in

the size distribution in the near wall region has a small effect on the size distribution at the wake, mainly because the boundary layer is thin.

Even though the numerical uncertainty analysis is not conclusive, the limited number of tests performed to the present show that the grids needed for polydisperse two-phase calculations have to be at least the same size as the single-phase grids if we want to properly describe the breakup, coalescence and dissolution rates in the near-wall regions. Thus, to run model-scale cases ($Re \backsim 2 \times 10^7$) we will need grids on the order of 500,000 nodes.

6. Conclusions and further work

A three dimensional polydisperse two-fluid model was presented. The model was used to calculate the two-phase bubbly flow around a surface ship assuming zero Froude number (i.e. ignoring the free surface deflection) and scaled Reynolds number. Air bubbles were introduced using a simulated breaking bow wave air bubble entrance boundary condition. From the analysis of the results, it follows that the intergroup transfer mechanisms play an important role in the determination of the two-phase flow field and the size distribution. The predictions show the relative importance of the intergroup transfer mechanisms and demonstrate the possibility that breaking wave actions near the blow of the ship can have a significant effect on the wake.

Much work is still needed to obtain reliable quantitative results for the polydisperse two-phase bubble field around a ship. First, the air entrainment boundary conditions must be determined in terms of variables involved in the solution of the problem, such as wave height, wave steepness, velocity gradients, turbulence, propeller characteristics, etc. Valid models relating the air entrainment to the problem variables is not yet available, and more experimental work is needed to be performed to obtain it. Second, there is much work to do to obtain validated kernels for coalescence and breakup. Lastly, some refinements are needed in the model for dissolution.

Even though the collision kernels are rather well studied and understood, mainly due to their application in coagulation kernels for aerosols (Williams and Loyalka, 1991), the probability of coalescence needs some refinements if we are to have a reliable predictive tool. The coalescence rate, and, in our case, the resulting two-phase flow, is highly dependent on the minimum contact time needed for coalescence, therefore, this parameter, mainly in terms of its dependence on surfactants, needs more accurate modeling. In addition, due to the presence of surfactants, coalescence may be inhibited in the ocean and then the formation of clusters of bubbles becomes possible, principally in the near-hull region where bubbles tend to accumulate. As clusters can not be treated the same way as bubbles, more work in this area is necessary.

In the case of the breakup of small bubbles under velocity gradients, there exists a criterion to estimate the minimum radius for breakup. Nevertheless, to the knowledge of the authors, no study exists relating the breakup frequency to the flow and bubble parameters. In addition, the model for bubble tipstreaming is inadequate, since only a few experiments have been done and almost no quantitative data are available. In every case, the effect of different parameters, such as turbulence and void fraction, and bubble breakup in the presence of strong velocity

gradients, needs to be studied. Additionally, it must be noticed that proper discretization in the near-wall region is necessary to predict the velocity gradients that strongly influence the breakup rate. This will require the use of dense grids in the boundary layer or proper modeling of the breakup terms in this region if a wall law together with a two-equation turbulence model is to be used. Furthermore, in the case of higher Reynolds number flows, the turbulence induced breakup could be significant.

It may be necessary to relax the assumption in the dissolution modeling that the concentration of dissolved air in water is the concentration at saturation at atmospheric pressure. The additional dissolution of air bubbles can appreciably increase the concentration of air in the liquid, thereby decreasing the dissolution rate. This may be important in the near hull region and near the propeller. To account for this effect, it would be necessary to add a new conservation equation to calculate the air concentration in the liquid.

Finally, the Baldwin–Lomax turbulence model is overly simple, and while it is probably adequate for predicting the wave structure around ships, it is not appropriate for bubble dispersion. In this model, the turbulent kinetic energy and its dissipation are not available and are coarsely estimated. Errors in the turbulent kinetic energy dissipation may also lead to incorrect estimations of the coalescence and breakup frequencies due to turbulence. The implementation of a two-equation turbulence model for two-phase flow is the next improvement on this regard.

In spite of all the modeling uncertainties, the three-dimensional polydisperse multigroup model presented herein for bubbly flow around a ship has demonstrated that the main features of the two-phase flow and bubble size distribution of the bubbly flow around a surface ship can be predicted.

Acknowledgements

This research was sponsored by the Office of Naval Research under grants N00014-91-J-1271 and N00014-96-I-0479; Dr Edwin Rood was the technical monitor. We also wish to acknowledge the help provided by Dr E. G. Paterson, Prof F. Stern and Dr M. Hyman. The computations were performed on the Cray C90 supercomputer at the Naval Oceanographic Supercomputer Center.

References

Acrivos, A., 1983. The breakup of small drops and bubbles in shear flows. Ann. New York Acad. Sci. 404, 1–11.

Alajbegovic, A., 1994. Phase distribution and turbulence structure for solid/fluid upflow in a pipe. Ph.D. thesis, Rensselaer Polytechnic Institute, Troy, NY.

Arnold, G.S., 1988. Entropy and objectivity as constraints upon constitutive equations for two-fluid modeling of multiphase flow. Ph.D. thesis, Rensselaer Polytechnic Institute, Troy, New York.

Baldwin, B.S., Lomax, H., 1978. Thin layer approximation and algebraic model for separated turbulent flow. AIAA 16th Aerospace Sciences Meeting , AIAA paper 78–257.

Bonetto, F., Lahey, R.T., Jr, 1993. An experimental study on air carryunder due to a plunging liquid jet. Int. J. Multiphase Flow 19, 281–294.

Carrica, P.M., Bonetto, F., Drew, D.A., Lahey, R.T., Jr, 1998. The interaction of background ocean air bubbles with a surface ship. Int. J. Num. Meth. Fluids 28, 571–600.

Cartmill, J.W., Su, M.Y., 1993. Bubble size distribution under saltwater and freshwater breaking waves. Dynamics Atmos. Oceans 20, 25–31.

Chesters, A.K., Hoffman, G., 1982. Bubble coalescence in bubble reactors and absorbers. Appl. Sci. Res. 38, 353–361.

Clift, R., Grace, J.R., Weber, M.E., 1978. Bubbles, Drops and Particles. Academic Press, New York.

Coulaloglou, C.A., Tavlarides, L.L., 1976. Drop size distribution and coalescence frequencies of liquid–liquid dispersions in flow vessels. AIChE J. 22, 289–297.

Day, W.G., Hurwitz, R.B., 1980. Propeller-disk wake survey data for model 4989 representing the FF 1052-class ship in a turn and with a bass dynamometer boat. DTNSRDC/SPD-011-21.

De Buijn, R.A., 1993. Tipstreaming of drops in simple shear flows. Chem. Eng. Sci. 48, 277–284.

Delhaye, J.M., 1981. J.M. Delhaye, M. Giot, M.L. Riethmuller (Ed.). Thermohydraulics of Two-Phase Systems for Industrial Design and Nuclear Engineering, Chaps 5, 78 and 9. Hemisphere, New York.

Drew, D.A., Lahey, R.T., Jr, 1979. Application of general constitutive principles to the derivation of multidimensional two-phase flow equations. Int. J. Multiphase Flow 5, 243–264.

Drew, D.A., Lahey, R.T., Jr, 1987. The virtual mass and lift force on a sphere in rotating and straining inviscid flow. Int. J. Multiphase Flow 13, 113–121.

Drew, D.A., Lahey, R.T., Jr, 1990. Some supplement analysis on the virtual mass and lift force on a sphere in rotating and straining inviscid flow. Int. J. Multiphase Flow 16, 1127–1130.

Ferziger, J.H., Kaper, H.G., 1972. Mathematical Theory of Transport Processes in Gases. North Holland, New York.

Guido, Lavalle G., Carrica, P.M., Clausse, A., Qazi, M.K., 1994. A bubble number density constitutive equation. Nucl. Engng. Des. 152, 213–224.

Hinze, J.O., 1955. Fundamentals of the hydrodynamic mechanism of splitting in dispersion processes. AIChE J. 1, 289–303.

Hyman, M., 1994. Modeling ship microbubble wakes. CSS/TR-94/39.

Ishii, M. 1975. Thermo-Fluid Dynamic Theory of Two-Phase Flow. Eyrolles, Paris.

Ishii, M., 1987. Two-fluid model for two-phase flow. Second International Workshop on Two-Phase Flow Fundamentals. Rensselaer Polytechnic Institute, Troy, NY.

Kirkpatrick, R.D., Locket, M.J., 1974. The influence of approach velocity in bubble coalescence. Chem. Eng. Sci. 29, 2363–2373.

Lahey, R.T. Jr, Drew, D.A., 1990. The current state-of-the-art in modeling of vapor/liquid two-phase flows. ASME paper-90-WA/HT-13.

Lance, M., Bataille, J., 1991. Turbulence in the liquid phase of a uniform bubbly air-water flow. J. Fluid Mech. 22, 95–118.

Levich, V.G., 1962. Physicochemical Hydrodynamics. Prentice–Hall, New York.

Loth, E., DeAngelis, B. 1996. Model of two-phase turbulent dispersion in a planar free shear layer. UILU report ENG 96-505/AAE report 96-05.

Luo, H., Svendsen, H.F., 1996. Theoretical model for drop and bubble breakup in turbulent dispersions. AIChE J. 42, 1225–1233.

Marrucci, G., 1969. A theory of coalescence. Chem. Eng. Sci. 24, 975–985.

Melville, W.K., 1996. The role of surface-wave breaking in air–sea interaction. Ann. Rev. Fluid Mech. 28, 279–325.

Miksis, M.J., 1981. A bubble in an axially symmetric shear flow. Phys. Fluids 24, 1229–1231.

Navarro-Valenti, S., Clausse, A., Drew, D.A., Lahey, R.T., Jr, 1991. A contribution to the mathematical modeling of bubbly/slug flow regime transition. Chem. Engng Comm. 102, 69–78.

Park, J.W., 1992. Void wave propagation in two-phase flow. Ph.D. thesis, Rensselaer Polytechnic Institute, Troy, New York.

Patankar, S.V., 1980. Numerical Heat Transfer and Fluid Flow. Hemisphere, New York.

Paterson, E.G., Hyman, M., Stern, F., Carrica, P.M., Bonetto, F., Drew, D.A., Lahey, R.T. Jr. 1996. Near and far-field CFD for a naval combatant including thermal-stratification and two-fluid modeling. Proceedings of the 21st Symposium on Naval Hydrodynamics. Trondheim, Norway. National Academy Press, Washington, DC.

Prince, M.J., Blanch, H.W., 1990. Bubble coalescence and breakup in air-sparged bubble columns. AIChE J. 36, 1485–1499.

Ramkrishna, D., 1985. The status of population balances. Rev. Chem. Eng. 3, 49–95.

Rattcliffe, T., Lindenmuth, W.T., 1990. Kelvin-wake measurements obtained on five surface ship models. DTRC-89/038.

Roe, P., 1985. Some contributions to the modelling of discontinuous flows. Large-Scale Computations in Fluid Mechanics. AMS, Providence, Rhode Island.

Rumscheidt, F.D., Mason, S.G. 1961. Particle motions in sheared suspensions XII. Deformation and burst of liquid drops in shear and hyperbolic flows. J. Colloid Sci. 16. 238–261.

Sanz, D., 1993. Una Contribución a la Formulación Geométrica-Estadística de la Topología del Flujo Bifásico. Master thesis, Universidad Nacional de Cuyo, Argentina.

Sanz, D., Guido, Lavalle G., Carrica, P.M., Clausse, A., 1995. About the statistical description of gas–liquid flows. In: Proceedings of the 7th International Meeting on Nuclear Reactor Thermal-Hydraulics. Saratoga Springs, U.S.A.

Sato, Y., Sadatomi, M., Sekoguchi, K., 1981. Momentum and heat transfer in two-phase bubbly flow—I. Int. J. Multiphase Flow 7, 167–177.

Saxena, S.K., Ravi, K., 1995. Computation of three dimensional supersonic and hypersonic blunt body flows using high resolution TVD schemes based on Roe's approximate Riemann solver. Lecture Notes Phys. 453, 520–533.

Smith, R.W., Hyman, M.C., 1987. Convective diffusive bubble transport in ship wakes. NCSC technical note 857–87.

Stern, F., Paterson, E.G., Tahara, Y., 1996. CFDSHIP-IOWA: computational fluid dynamics method for surface-ship boundary layers and wake and wave fields. Iowa Institute of Hydraulic Research Report 666, Iowa City.

Stone, H.A., 1994. Dynamics of drop deformation and breakup in viscous fluids. Ann. Rev. Fluid Mech. 26, 65–102.

Sweby, P.K. 1985. High resolution TVD schemes using flux limiters. In: Large-Scale Computations in Fluid Mechanics. AMS, Providence, Rhode Island.

Tamamidis, P., Assanis, D.N., 1993. Evaluation of various high-order accuracy schemes with and without flux limiters. Int. J. Num. Meth. Fluids 16, 931–948.

Taylor, G., 1934. The formation of emulsions in definable field of flow. Proc. Roy. Soc. A 146, 501–523.

Tahara, Y., Stern, F., Rosen, B., 1992. An interactive approach for calculating ship boundary layers and wakes for nonzero Froude number. J. Comp. Phys. 98, 33–53.

Thomas, R.M., 1981. Bubble coalescence in turbulent flows. Int. J. Multiphase Flow 7, 709–717.

Thompson, J.F., 1982. General curvilinear coordinate systems. Appl. Math. Comp. 10, 1–30.

Wang, S.K., Lee, S.J., Jones, O.C., Lahey, R.T., Jr, 1987. 3-D turbulence structure and phase distribution measurements in bubbly two-phase flow. Int. J. Multiphase Flow 13, 327–343.

Williams, M.M.R., Loyalka, S.K., 1991. Aerosol Science Theory and Practice. Pergamon Press, Oxford.